

July 24, 2013
DRAFT

Thermal Modeling of Disordered Materials

Jason M. Larkin

August 2013

School of Computer Science
Carnegie Mellon University
Pittsburgh, PA 15213

Thesis Committee:

Alan J. H. McGaughey, Chair
Jonathan Malen
Craig Maloney
Michael Widom

*Submitted in partial fulfillment of the requirements
for the degree of Doctor of Philosophy.*

July 24, 2013
DRAFT

Keywords: Phonon

Acknowledgments

D) Acknowledgments must include financial support acknowledgment as discussed in Section 5

July 24, 2013
DRAFT

July 24, 2013
DRAFT

Abstract

E) Abstract should not exceed 350 words; see Section 2

July 24, 2013
DRAFT

Contents

1	Introduction	1
1.1	new section	1
2	Predicting alloy vibrational mode properties using lattice dynamics calculations, molecular dynamics	4
2.1	Introduction	4
2.2	Theoretical and Computational Framework	5
2.2.1	Thermal Conductivity Prediction	5
2.2.2	Virtual Crystal Approximation	6
2.2.3	Calculation and Simulation Details	8
2.3	Vibrational Mode Properties in Alloys	8
2.3.1	Density of States	8
2.3.2	Dispersion and Group Velocity	11
2.3.3	Lifetimes	14
2.3.4	Diffusivities	20
2.3.5	Discussion	22
2.4	Thermal Conductivity Prediction	22
2.5	SW silicon	26
2.6	Summary	29
3	Vibrational Mean Free Paths and Thermal Conductivity Accumulation Functions for Amorphous Ma	31
3.1	new section	31
4	Origin of the Exceptionall Low Thermal Conductivity of PCBM Thin Films	33
4.1	new section	33
5	Conclusion	35
5.1	new section	35
A	Vibrational Lifetimes from Molecular Dynamics	37
A.1	Introduction	37
A.2	Phonon Spectral Energy Density	39
A.2.1	As Derived from Normal Mode Coordinates, Φ	39
A.3	Derivation of Phonon Spectral Energy Density, Φ	39
A.3.1	Alternative Formulation, Φ'	43

A.4	Interpretation of Φ'	44
A.5	NMD using Non-Exact Normal Modes	45
A.6	Computational Details	45
A.6.1	Allowed Wavevectors	45
A.6.2	Symmetry Discussion	47
A.6.3	Phonon Lifetimes and Frequencies	47
A.6.4	Thermal Conductivity	49
A.7	Finite Simulation-Size Scaling for Thermal Conductivity	49
A.7.1	Computational Cost	50
A.8	Case Studies	51
A.8.1	Lennard-Jones Argon	51
A.8.2	Stillinger-Weber Silicon	55
A.8.3	Carbon Nanotube	56
A.9	Summary	57
B	Research using High Performance Computing	59
B.1	Setting Up Computing Environment	59
B.1.1	Hardware and Operating System Choice	59
B.1.2	System Terminal and Commands	59
B.1.3	Environment Variables	59
B.1.4	Shell Scripts and System Commands in Python	60
B.1.5	Remote Resources Commands	60
B.1.6	Installing Programs	60
B.1.7	Available Programs	61
B.2	Preparing Journal Articles and Thesis	61
B.2.1	Journal Articles	62
B.2.2	Thesis	62
B.3	Technical Advice	62
B.3.1	Expert Advice	62
B.3.2	Online Resources	63
B.4	Coding Languages: Compiled versus Interpreted	63
B.4.1	Compiled Language Case-study: Lennard-Jones Argon Molecular Dynamics	63
B.4.2	Compiled versus Interpreted Case-study(a): Lennard-Jones Dispersion	64
B.4.3	Compiled versus Interpreted Case-study(b): Allen-Feldman Diffusivity Calculation	64
B.4.4	Scaling Calculations	65
Bibliography		67

List of Figures

- 2.1 (a) Explicitly disordered alloy supercell of silicon and “heavy” silicon ([100] direction into the page).
- 2.2 Vibrational DOS for LJ alloys calculated using the VC approximation and an explicitly disordered supercell.
- 2.3 Left and right panels: The structure factor for longitudinal (S_L) and transverse (S_T) polarizations along the [100] direction.
- 2.4 Lifetimes predicted using VC-NMD and Gamma-NMD from MD simulations of (a) perfect LJ argon and (b) LJ argon alloy.
- 2.5 (a) Predicted lifetimes using VC-NMD and VC-ALD for LJ argon ($T = 10$ K, $N_0 = 10$, and $c = 0.05$).
- 2.6 AF theory predictions of disordered mode diffusivities for LJ argon alloy and amorphous phases. The ω axis is in cm⁻¹.
- 2.7 Thermal conductivity predictions for LJ argon and alloys at $T=10$ K using the VC-NMD, VC-ALD, and AF theories.
- 2.8 (a) Predicted lifetimes using VC-NMD and VC-ALD for SW silicon ($T = 300$ K, $N_0 = 8$, and $c = 0.05$).
- 2.9 Thermal conductivity predictions for SW silicon and alloys at a temperature of 300 K using the VC-ALD theory.

- A.1 The normal mode kinetic energy, Φ , of two modes (A and B) at wavevector [0.25 0 0] calculated using the VC approximation.
- A.2 The SED (using Φ) for the first three polarizations at the wavevector [$\pi/4a, \pi/4a, \pi/4a$] for LJ argon and silicon.
- A.3 Thermal conductivity predictions for LJ argon calculated using phonon lifetimes predicted by Φ and Φ' .
- A.4 The phonon spectral energy density (Φ) is plotted as larger blue circles. The proposed alternative expression is shown as smaller red circles.
- A.5 Comparison of the phonon frequencies and lifetimes predicted using $\Phi(\omega)$ and τ and $\Phi'(\omega')$ and τ' for a (8,8) supercell.
- A.6 Comparison of the phonon frequencies and lifetimes predicted using $\Phi(\omega)$ and τ and $\Phi'(\omega')$ and τ' for a (16,16) supercell.
- A.7 Comparison of the phonon frequencies and lifetimes predicted using $\Phi(\omega, \tau)$ and $\Phi'(\omega', \tau')$ for a (8,8) supercell.

July 24, 2013
DRAFT

List of Tables

2.1 Thermal conductivity predictions using the VC-NMD, VC-ALD, and GK methods. For LJ argon alloy

A.1 Thermal conductivity values in W/m-K predicted using the Φ , Φ' , and Green-Kubo methods. The pred

July 24, 2013
DRAFT

Chapter 1

Introduction

There are two sections to this introductory chapter.

1.1 new section

test section

July 24, 2013
DRAFT

Chapter 2

Predicting alloy vibrational mode properties using lattice dynamics calculations, molecular dynamics simulations, and the virtual crystal approximation

The virtual crystal (VC) approximation for mass disorder is evaluated by examining two model alloy systems: Lennard-Jones argon and Stillinger-Weber silicon. In both material systems, the perfect crystal is alloyed with a heavier mass species up to equal concentration. The analysis is performed using molecular dynamics simulations and lattice dynamics calculations. Mode frequencies and lifetimes are first calculated by treating the disorder explicitly and under the VC approximation, with differences found in the high-concentration alloys at high frequencies. Notably, the lifetimes of high-frequency modes are underpredicted using the VC approximation, a result we attribute to the neglect of higher-order terms in the model used to include point-defect scattering. The mode properties are then used to predict thermal conductivity under the VC approximation. For the Lennard-Jones alloys, where high-frequency modes make a significant contribution to thermal conductivity, the high-frequency lifetime underprediction leads to an underprediction of thermal conductivity compared to predictions from the Green-Kubo method, where no assumptions about the thermal transport are required. Based on observations of a minimum mode diffusivity, we propose a correction that brings the VC approximation thermal conductivities into better agreement with the Green-Kubo values. For the Stillinger-Weber alloys, where the thermal conductivity is dominated by low-frequency modes, the high-frequency lifetime underprediction does not affect the thermal conductivity prediction and reasonable agreement is found with the Green-Kubo values.

2.1 Introduction

Due to their potentially low thermal conductivities, disordered materials (e.g., alloys, amorphous solids, aerogels) are used in applications ranging from thermoelectric energy conversion to thermally insulating barriers. [5, 6, 7, 8, 9, 10, 11, 12, 13, 14] Disordered lattices are a subgroup of disordered materials where the atomic positions follow a lattice structure but the constituent species are spatially random. Examples include isotopic solids, where the species have the same electronic structure but small mass variations,[15, 16] and alloys, our focus here, where at least two distinct species are present.[17, 18]

We further restrict our focus to dielectric or semiconducting solids, where the heat is conducted by the atomic vibrational modes. Predicting the thermal conductivity of such materials requires the properties of the full spectrum of vibrational modes. [19, 20, 21] Accurate predictions of these properties for crystalline systems (i.e., perfect lattices) can be made with anharmonic lattice dynamics (ALD) theory using input from density functional theory (DFT) calculations.[16, 22, 23, 24, 25, 26, 27, 28, 29, 30] Computational costs limit DFT calculations to less than 100 atoms, however, making it challenging to explicitly incorporate the effects of disorder. [16, 24, 26, 29, 31, 32, 33]

Disorder is typically included in the ALD framework using Abeles' virtual crystal (VC) approximation, whereby the disordered solid is replaced with a perfect VC with properties equivalent to an averaging over the disorder (e.g., atomic mass, bond strength).[18] The ALD calculations are performed on a small unit cell with the averaged properties (i.e., all vibrational modes are phonons) and phonon-phonon and phonon-disorder scattering are included as perturbations. [15, 16, 18, 24, 26] Except for low-frequency (long-wavelength) acoustic modes, the general validity of this assumption is unclear. We will refer to this approach as VC-ALD. Recent work using DFT calculations and the VC-ALD approach has modeled disordered lattices with relatively large ($\sim 10\text{-}100 \text{ W/m-K}$) [16, 24, 29] and small ($\sim 1 \text{ W/m-K}$)[26] thermal conductivities. No comprehensive study has been performed to assess the applicability of the VC-ALD approach for a range of disorder strength.

The objective of this study is to investigate the use of the VC approximation for predicting the vibrational mode properties and thermal conductivity of alloys by a detailed comparison of three predictive methods: (i) molecular dynamics (MD)-based normal mode decomposition (NMD), (ii) MD-based Green-Kubo (GK), and (iii) VC-ALD. By using computationally-inexpensive empirical potentials for argon [Lennard-Jones (LJ) at a temperature of 10 K] [34] and silicon [Stillinger-Weber (SW) at a temperature of 300 K], [35] we can self-consistently study the effects of disorder both explicitly and as a perturbation. For both materials, the perfect lattice is disordered with a heavier mass species up to equal concentration, spanning a range of small to large disorder. By spanning this range, the limits of the perturbative models are examined.

The remainder of the paper is organized as follows. In Section 2.2, the theoretical formulation of thermal transport in ordered and disordered solids and the computational framework are described. In Section 2.3, the frequencies, group velocities, lifetimes, and diffusivities of the vibrational modes of the LJ argon alloys are predicted when the disorder is explicitly modeled and when it is treated as a perturbation in the VC approximation. A breakdown of the VC-ALD method is identified by a comparison with the VC-NMD method in Section 2.3.3 and a correction is suggested in Section 2.3.4. The vibrational mode properties are then used to predict thermal

conductivities in Section 2.4, allowing for a comparison to the predictions of the top-down GK method, where no assumptions about the nature of the thermal transport are required. The vibrational mode properties and thermal conductivity of the SW silicon alloys, where low-frequency modes dominate the thermal conductivity, are predicted in Section 2.5 to provide a comparison and contrast to the LJ argon alloys.

2.2 Theoretical and Computational Framework

2.2.1 Thermal Conductivity Prediction

To predict the thermal conductivity of a disordered lattice, one begins with the theory for a perfect lattice. For a perfect lattice, all vibrational modes are phonon modes, which by definition are delocalized, propagating plane waves. [19] Using the single-mode relaxation time approximation [19] to solve the Boltzmann transport equation gives an expression for thermal conductivity in direction \mathbf{n} ,

$$k_{ph,\mathbf{n}} = \sum_{\boldsymbol{\kappa}} \sum_{\nu} c_{ph}(\boldsymbol{\kappa}) v_{g,\mathbf{n}}^2(\boldsymbol{\kappa}) \tau(\boldsymbol{\kappa}). \quad (2.1)$$

Here, the sum is over the phonon modes in the first Brillouin zone, $\boldsymbol{\kappa}$ is the wave vector, and ν labels the polarization branch. The phonon mode has frequency $\omega(\boldsymbol{\kappa})$, volumetric specific heat $c_{ph}(\boldsymbol{\kappa})$, \mathbf{n} -component of the group velocity vector $v_{g,\mathbf{n}}(\boldsymbol{\kappa})$, and lifetime $\tau(\boldsymbol{\kappa})$.

The relaxation time approximation has been found to be valid for lower thermal conductivity materials (e.g., Si and SiGe alloys), [22, 23, 24] while larger thermal conductivity materials such as GaN and diamond require an iterative solution to the BTE for more accurate predictions using Eq. (2.1). [16, 31] For the crystalline LJ argon and SW silicon phases, the lattices and the components of their thermal conductivity tensors are cubically symmetric, so that we will refer to k_{ph} as an isotropic scalar thermal conductivity. This isotropy will hold for disordered lattices in the infinite-size limit. Since MD simulations are classical and obey Maxwell-Boltzmann statistics,[36] the volumetric specific heat is k_B/V per mode in the harmonic limit, where V is the system volume and k_B is the Boltzmann constant. This harmonic approximation for specific heat has been shown to be valid for LJ argon and SW silicon at the temperatures of interest here [37, 38] and is used so that direct comparisons can be made between the MD- and lattice dynamics-based methods.

For disordered systems, the vibrational modes are no longer pure plane-waves (i.e., phonon modes), except in the low-frequency (long-wavelength) limit. When applied in the classical limit, the Allen-Feldman (AF) theory computes the contribution of diffusive, non-propagating modes (i.e., diffusons) to thermal conductivity from[39]

$$k_{AF} = \sum_{diffusons} \frac{k_B}{V} D_{AF,i}(\omega_i), \quad (2.2)$$

where $D_{AF,i}$ is the mode diffusivity and ω_i is the frequency of the i th diffuson. The diffusivity of diffusons can be calculated from harmonic lattice dynamics theory. [20, 39, 40]

Assuming that all vibrational modes travel with the sound speed, v_s , and scatter over a distance of the lattice constant, a , a high-scatter (HS) limit of thermal conductivity in the classical limit is[6]

$$k_{HS} = \frac{k_B}{V_b} b v_s a, \quad (2.3)$$

where V_b is the volume of the unit cell and b is the number of atoms in the unit cell. The HS limit will be used to discuss the differences between the LJ argon and SW silicon alloys.

2.2.2 Virtual Crystal Approximation

Under the VC approximation, the disordered solid is replaced with a perfect, single-species crystal with properties (e.g., density, cohesive energy) equivalent to an averaging over the disorder (e.g., atomic mass, bond strength).[18] The VC approximation is visualized for an alloy in Figs. 2.1(a) and 2.1(b), where a mass-disordered supercell is replaced by a perfect crystal with an averaged mass. Abeles first introduced the concept of a VC to predict the thermal conductivity of SiGe, GaAs/InAs, and InAs/InP alloys. [18] Klemens-Callaway theory, which is valid for low-frequency modes and small disorder, was used to model the phonon-phonon and phonon-defect scattering. [18, 41, 42, 43, 44, 45] The Abeles theory is conceptually simple, treating both disorder and anharmonicity as perturbations, and leads to a closed-form analytical function for the thermal conductivity. With the use of phenomenological fitting parameters, good agreement between the predictions and experimental measurements was found for SiGe and GaAs/InAs alloys. Deviations were observed for InAs/InP alloys at large concentrations of InP, which were attributed to the large mass ratio of 3.7 between indium and phosphorus.[18]

When considering alloys, it is important to note that the overall disorder strength is determined by the mass ratio, the stiffness ratio, and the alloy concentration. Cahill and co-workers found that as little as $6.2 \times 10^{19} \text{ cm}^{-3}$ germanium reduces the thermal conductivity of epitaxial silicon layers by a factor of two. [46] Using the Abeles theory, they explained this result by mass perturbative disorder alone (the Ge/Si mass ratio is 2.6). [46, 47] The relative effects of bond and mass disorder were investigated computationally using MD simulations by Skye and Schelling for SiGe alloys up to equal concentration. [48] They also found that mass disorder is the dominant scattering mechanism. Subsequent studies have modeled the effect of differing species by only including atomic mass differences.[49, 50]

Unlike the phenomenological Abeles theory, the VC-ALD approach predicts thermal conductivity by directly summing over the modes of the full vibrational spectrum, with phonon-phonon and phonon-defect scattering treated as perturbations. [16, 24, 26] In the VC-ALD method, the phonon-phonon scattering is predicted using ALD.[3, 28] The phonon-defect scattering is treated using perturbative methods that can handle mass and/or bond disorder. [15, 41, 42, 44] In $\text{Ni}_{0.55}\text{Pd}_{0.45}$, which has a large mass ratio (1.8) and concentration of each species, experimental measurements of vibrational frequencies and linewidths agree well with predictions from the perturbative mass-disorder theory. [15, 44, 45]

Using DFT methods to predict the mode-specific phonon properties of the VC, Lindsay and Broido found good agreement between VC-ALD and experimental measurements of thermal conductivity for isotopically defected GaN (the gallium isotopes have concentrations of 0.6 and 0.4 and a mass ratio of 1.03).[16] Garg et al. used DFT calculations with VC-ALD to predict the

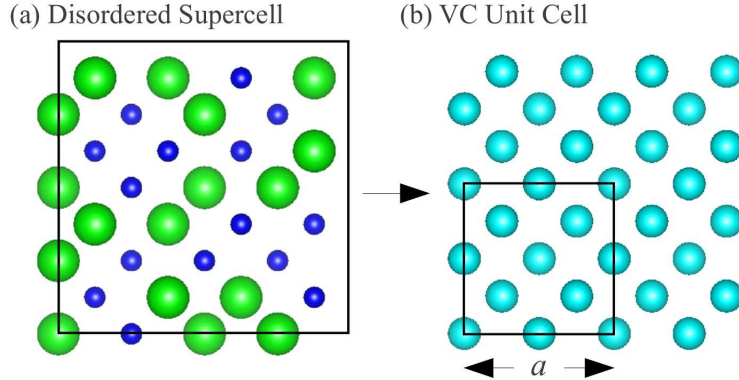


Figure 2.1: (a) Explicitly disordered alloy supercell of silicon and “heavy” silicon ([100] direction into the page). [1] (b) Equivalent VC supercell with one averaged mass. The sphere size represents increasing mass only, no bond disorder is considered. The 8-atom conventional cubic unit cell is shown in (b).

thermal conductivity of SiGe alloys for all concentrations at a temperature of 300 K, obtaining good agreement with experiment.[24] By including disorder explicitly in their ALD calculations, the predicted thermal conductivity decreased by 15%. Isotopically-defected GaN and low concentration SiGe alloys have relatively large thermal conductivities at a temperature of 300 K (~ 100 W/m-K). Li et al. used DFT calculations with VC-ALD to predict the thermal conductivity of $Mg_2Si_xSn_{1-x}$ (~ 10 W/m-K) in good agreement with experimental measurements for all concentrations.[29] The VC-ALD approach has also been used to predict the effect of interfacial mixing in GaAs/AlAs superlattices, but the thermal conductivity predictions were not compared with experimental measurements.[30] In our survey of experimental measurements and numerical modeling, we find that VC predictions tend to be accurate when the disordered lattice thermal conductivity is significantly above the high-scatter limit [Eq. (2.3)], which tends to be around 1 W/m-K. [6, 16, 18, 24, 45, 46, 47]

An ALD study using phonon properties from DFT calculations for crystalline PbTe[25] predicted thermal conductivities of 2 W/m-K at a temperature of 300 K in fair agreement with experiment. For PbTeSe alloys, a VC-ALD study predicted a small thermal conductivity reduction compared to the perfect crystals.[26] Experimental results are limited for these alloys,[51, 52] making it difficult to assess the validity of the VC-ALD approach for materials whose thermal conductivities approach the high-scatter limit.

Given all these results, it is unclear what limitations exist for using the VC approach. In this study, we will consider a low thermal conductivity alloy using the LJ potential and a high thermal conductivity alloy using the SW potential. The computational studies discussed above were limited to VC-ALD because of DFT calculation costs. Our use of computationally inexpensive empirical potentials allows us to include the disorder explicitly and as a perturbation and to compare the predictions.

2.2.3 Calculation and Simulation Details

The key to explicitly incorporating the effects of disorder is to use large disordered supercells. Perfect and disordered lattice supercells are generated using the conventional unit cells for LJ argon ($n = 4$) and SW silicon ($n = 8$), where n is the number of atoms in the unit cell. Supercells are built cubically with size N_0 , where N_0 is the number of unit cell repetitions in the three spatial directions. Supercells up to $N_0 = 12$ (6,096 atoms) are used for the LJ argon calculations. For SW silicon, $N_0 = 8$ (4,096 atoms) is used for the MD-based NMD calculations and $N_0 \leq 42$ (592,704 atoms) is used for the MD-based GK and VC-ALD.

Disorder is created by randomly specifying the masses of the atoms on the lattice. The composition of each lattice is labeled by $m_{1-c}^i m_c^j$, where (i) $m^i = 1$ and $m^j = 3$ in LJ units for argon, and (ii) $m^i = m_{Si}$ and $m^j = 2.6m_{Si}$ for SW silicon and “heavy silicon”, which has the mass of germanium. Concentrations, c , of 0, 0.05, 0.15 and 0.5 are considered.

For LJ argon, the lattice constant at a temperature of 10 K is 5.290 Å.[53] The MD simulations were performed using LAMMPS.[54] Efficient MD codes like LAMMPS scale linearly with the number of atoms in the system, N_a , which makes the GK method (see Section 2.4) computationally-inexpensive when used with empirical potentials. An amorphous LJ phase, discussed in Section 2.3.4, was created by liquefying the crystal and instantly quenching by removing all kinetic energy. The energy of the resulting structure was minimized and then annealed in an *NPT* (constant number of atoms N , pressure P , and temperature T) ensemble at zero pressure and a temperature of 10 K. The effective zero-pressure lattice constant of the amorphous phase at this temperature, based on the atomic density, is 5.389 Å. For SW silicon, we use a lattice constant of 5.43 Å for all calculations, which brings the perfect crystal GK thermal conductivity predictions at a temperature of 300 K [38, 55] into better agreement with ALD predictions[56] compared to using the zero-pressure lattice constant.

All MD simulations are first equilibrated in a *NVT* (constant number of atoms, volume, and temperature) ensemble for 10^6 time steps. Data is then collected from simulations in the *NVE* (constant number of atoms, volume, and total energy) ensemble. For LJ argon, the potential energy is cutoff and shifted at 8.5 Å (the force is not adjusted). Time steps of 4.285 and 0.5 fs were used for the LJ argon and SW silicon simulations. The same atomic trajectories are used for the NMD and GK methods.

2.3 Vibrational Mode Properties in Alloys

2.3.1 Density of States

In this section, we begin to examine the effects of explicitly including disorder by computing the frequencies and density of states (DOS) for the vibrational modes of disordered LJ lattice supercells and their equivalent VCs. The frequencies are computed using harmonic lattice dynamics calculations with GULP.[57] For the VC, the allowed wave vectors are set by N_0 and, due to the use of the conventional unit cell, there are 12 polarization branches per wave vector. For the disordered supercells (referred to herein as Gamma), the only allowed wave vector is the gamma-point (i.e., $\kappa = 0$), where there are $12N_0^3$ polarization branches. Calculation of the Gamma modes require the eigenvalue solution of a dynamical matrix of size $(3N_a)^2$ that

scales as $[(3N_a)^2]^3$, limiting the system sizes that can be considered. This eigenvalue solution is also required to perform the Gamma-NMD (see Section 2.3.3) and AF calculations (see Section 2.3.4).

The DOS for the VC and Gamma modes are plotted in Figs. 2.2(a), 2.2(b), and 2.2(c) for concentrations of 0.05, 0.15, and 0.5 for $N_0 = 12$ (6,912 atoms). The VC and Gamma DOS agree at low frequencies for all concentrations, where they follow the prediction of the Debye approximation that the DOS will scale as ω^2 .[34] Similar agreement between VC and Gamma DOS at low frequencies was found in DFT predictions for $\text{Si}_c\text{Ge}_{1-c}$ [24] and classical models of amorphous $\text{Si}_c\text{Ge}_{1-c}$. [58] The Debye approximation underpredicts the DOS at moderate frequency, which is due to non-linearities in the dispersion,[34] but the VC and Gamma predictions remain in good agreement.

The increasing average atomic mass with increasing concentration for the VC shifts all frequencies downward by a factor $1/[(1 - c)m^i + cm^j]^{1/2}$. The increasing average atomic mass for the Gamma modes also reduces the frequencies, but not in a systematic manner. The effect of the disorder is seen at frequencies greater than ten by a broadening and shift of the Gamma DOS to higher frequencies because of the explicit use of light atoms in the supercell. This effect becomes more pronounced as the concentration increases. Duda et al. observed similar high-frequency broadening effects in model LJ alloys. [59] The high-frequency broadening is an indication of phonon localization, which is known to first occur at the Brillouin zone edge.[60] Based on the DOS, the vibrational modes of the explicitly disordered supercells at low frequencies are propagating, while the broadening of the DOS at high-frequency indicates that the Gamma vibrational modes may differ from the VC phonon modes in this regime. This behavior is further investigated in the next three sections.

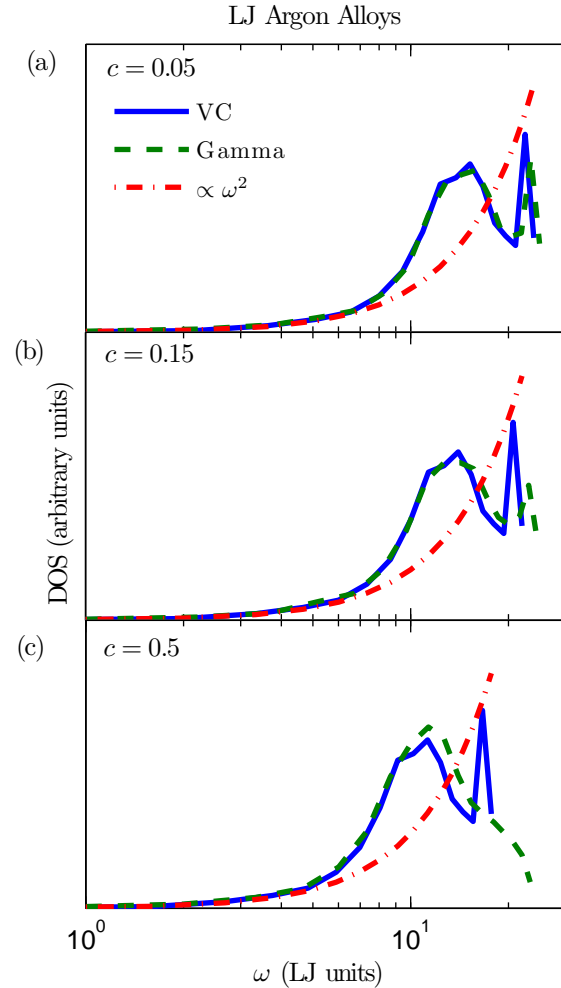


Figure 2.2: Vibrational DOS for LJ alloys calculated using the VC approximation and an explicitly disordered supercell (labeled Gamma) for concentrations of (a) 0.05, (b) 0.15, and (c) 0.5. VC and Gamma show similar low-frequency behavior for all concentrations. For increasing concentrations, the frequencies of both VC and Gamma decrease, while the high frequency DOS for Gamma spreads and reaches to a higher maximum frequency because of the explicit disorder. The supercells are of size $N_0 = 12$ (6,912 atoms).

2.3.2 Dispersion and Group Velocity

The group velocity vector in a VC is defined as the gradient of the dispersion curve,

$$\mathbf{v}_{g,\mathbf{n}}(\boldsymbol{\kappa}) = \frac{\partial\omega(\boldsymbol{\kappa})}{\partial\boldsymbol{\kappa}}. \quad (2.4)$$

We calculate the group velocities for the VC using finite differences on the frequencies calculated from harmonic lattice dynamics.[61]

For a disordered solid, the three acoustic group velocities (two transverse and one longitudinal) can be predicted using the elastic constants [57] or by finite differencing of the three lowest frequency branches of the dispersion relation of the supercell. [4, 62] Except for this low-frequency behavior, there is not an accepted method to predict the group velocity of a vibrational mode in a disordered system, although there have been attempts. [4, 6, 59, 62, 63, 64] In the Cahill-Pohl model, for example, the group velocity of all disordered modes is the sound speed, v_s , which is also assumed for the high-scatter model, Eq. (2.3). [6] This assumption is not generally valid for any material.[4, 40, 59, 62, 63, 64?]

Calculating the structure factors of the supercell Gamma modes is a method to test for their plane-wave character at a particular wave vector and polarization corresponding to the VC. [21, 40] Feldman et al. used the structure factor to predict an effective dispersion for a model of amorphous silicon, but did not predict group velocities.[40] Volz and Chen used the dynamic structure factor to predict the dispersion of crystalline SW silicon using MD simulation. [65] Recently, the effective dispersion of a model disordered lattice was predicted using the structure factor. [?]

The structure factor at a VC wave vector $\boldsymbol{\kappa}_{VC}$ is defined as[21]

$$S^{L,T} = \sum_{\nu} E^{L,T} \delta[\omega - \omega], \quad (2.5)$$

where the summation is over the Gamma modes, E^T refers to the transverse polarization and is defined as

$$E^L = \left| \sum_b \hat{\boldsymbol{\kappa}}_{VC} \cdot e \exp[i\boldsymbol{\kappa}_{VC} \cdot \mathbf{r}_0(l=0_{bb}, \alpha=0)] \right|^2 \quad (2.6)$$

and E^L refers to the longitudinal polarization and is defined as

$$E^T = \left| \sum_b \hat{\boldsymbol{\kappa}}_{VC} \times e \exp[i\boldsymbol{\kappa}_{VC} \cdot \mathbf{r}_0(l=0_{bb}, \alpha=0)] \right|^2. \quad (2.7)$$

In Eqs. (2.6) and (2.7), the b summations are over the atoms in the disordered supercell, $\mathbf{r}_0(l=0_{bb}, \alpha=0)$ refers to the equilibrium atomic position of atom b in the supercell, l labels the unit cells ($l = 0$ for the supercell), α labels the Cartesian coordinates, and $\hat{\boldsymbol{\kappa}}_{VC}$ is a unit vector. Explicit disorder is included in the Gamma frequencies ω and the $3N_a$ components of the eigenvectors, e .

Physically, $S^{L,T}$ represents the frequency spectrum required to create a wavepacket with a well-defined wave vector and polarization. [21, 40, 66] For a perfect lattice, the structure factor peaks are delta functions centered at the mode frequencies, indicating that the modes are pure

plane-waves (i.e., phonons). A sampling of the structure factors for the LJ argon alloys are plotted in Fig. 2.3 for wave vectors along the [100] and [111] directions in the $N_0 = 10$ systems.[?] Well-defined peaks at all wave vectors are due to the lattice structure of the disordered systems. Typically, the structure factor for amorphous materials has well-defined peaks only for small wave vector. [21, 40] With increasing disorder, the structure factor spreads in width, particularly at high frequencies, which is an indication that the modes are not pure plane waves.

From Fig. 2.3, an effective dispersion curve (middle panels) can be extracted by locating the peaks in the structure factors at neighboring VC wave vectors. The peaks in the structure factor are larger than the VC predicted frequencies (plotted as solid lines in Fig. 2.3) by at most 5%. Similar agreement is found with the disordered SW silicon lattice supercells.

Even though there is good agreement between the VC-predicted dispersion curves and the peaks in the structure factors from Fig. 2.3, the effect of the width of the peaks is not clear. We will use the group velocities predicted by the VC dispersion for both LJ argon and SW silicon in the VC-NMD and VC-ALD calculations for consistency and simplicity. The validity of this group velocity choice will be discussed in Section 2.3.5.

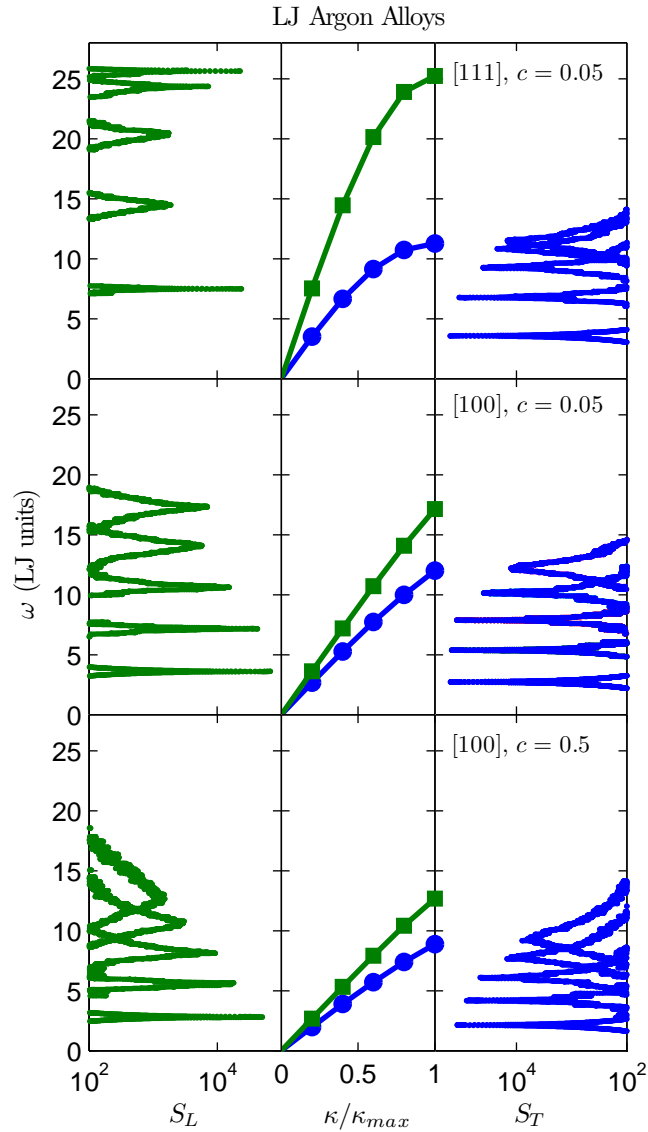


Figure 2.3: Left and right panels: The structure factor for longitudinal (S_L) and transverse (S_T) polarizations along high-symmetry directions of the mass disordered LJ argon supercells ($N_0 = 10$, $c = 0.05, 0.5$). Center panels: The VC predicted dispersion curves (solid lines) agree well with the locations of the peaks in S_L and S_T (data points). The wavenumber axis in the center panel is normalized by the maximum value of the wavenumber in the given direction.

2.3.3 Lifetimes

From VC-NMD and Gamma-NMD

Once the group velocities are predicted using the VC dispersion, the mode lifetimes are required to predict the thermal conductivity using Eq. (2.1). As an alternative to the VC-ALD approach for predicting lifetimes, which is discussed in the next section, we first use the MD simulation-based NMD method.[37, 67, 68, 69] In NMD, the atomic trajectories are first mapped onto the vibrational mode coordinate $q(\kappa_\nu; t)$ and its time derivative $\dot{q}(\kappa_\nu; t)$ by [70]

$$q(\kappa_\nu; t) = \sum_{\alpha, b, l}^{3,n,N} \sum_{\alpha, b}^{3,n} \sum_{\kappa, \nu}^{N, 3n} \sqrt{\frac{m_b}{N}} u_\alpha(l_b; t) e^*(\kappa_\nu^\alpha) \exp[i\kappa \cdot \mathbf{r}_0(l_{bb0})] \quad (2.8)$$

and

$$\dot{q}(\kappa_\nu; t) = \sum_{\alpha, b, l}^{3,n,N} \sum_{\alpha, b}^{3,n} \sum_{\kappa, \nu}^{N, 3n} \sqrt{\frac{m_b}{N}} \dot{u}_\alpha(l_b; t) e^*(\kappa_\nu^\alpha) \exp[i\kappa \cdot \mathbf{r}_0(l_{bb0})]. \quad (2.9)$$

Here, m_b is the mass of the b_{th} atom in the unit cell, u_α is the α -component of the atomic displacement from equilibrium, \dot{u}_α is the α -component of the atomic velocity, and t is time. The total energy of each vibrational mode, $E(\kappa_\nu; t)$, is calculated from

$$E(\kappa_\nu; t) = \frac{\omega(\kappa_\nu)^2}{2} q(\kappa_\nu; t)^* q(\kappa_\nu; t) + \frac{1}{2} \dot{q}(\kappa_\nu; t)^* \dot{q}(\kappa_\nu; t). \quad (2.10)$$

The vibrational mode lifetime is predicted using

$$\tau(\kappa_\nu) = \int_0^{t^*} \frac{E(\kappa_\nu; t)}{\langle E \rangle} dt, \quad (2.11)$$

where the upper integration limit t^* is set to be much larger than the mode lifetime and the brackets indicate an ensemble average.[69] The NMD calculations scale as $(N_a)^2$.[3]

We perform the MD simulations using the fully disordered supercells and project onto the frequencies and eigenvectors from both the VC unit cell [$\omega(\kappa_\nu)$, $e(\kappa_\nu^\alpha)$] and the Gamma supercell [ω , e]. Previous studies of disordered supercells with the NMD method have used the Gamma modes only to perform the projections. [55, 62, 63, 64, 71] The trajectories from the MD simulations are also used in the GK method calculations (Section 2.4). The MD simulations were ten times longer than the longest lifetime in the system, which was estimated from the VC-ALD predicted lifetimes. For LJ argon and SW silicon, data was collected for 2^{20} and 2^{22} time steps and the atomic trajectories were sampled every 2^8 and 2^4 time steps. Ensemble averaging of the energy autocorrelations was performed using ten independent, initially-randomized velocity distributions.

For the normal modes of the lattice supercell, where the energy autocorrelation follows an exponential decay,[67, 68] Eq. (2.11) is exact, but this expression becomes an approximation when using the VC normal modes to perform the mappings in Eqs. (2.8) and (2.9). Even for larger disorder ($c = 0.5$), where the energy autocorrelations deviate from an exponential decay,

an effective lifetime can still be predicted using Eq. (2.11) (see Appendix A.5). The lifetimes predicted using VC-NMD and Gamma-NMD are shown in Figs. 2.4(a)-2.4(d) for the LJ argon crystal and all alloys at a temperature of 10 K. The range of frequencies for VC-NMD and Gamma-NMD differ slightly due to differences in the DOS (see Fig. 2.2). For a small interval of frequency, there is a wider range of predicted lifetimes for Gamma-NMD. This spread is because there is no symmetry-averaging of the mode properties, which is possible for the VC by considering the crystal lattice's irreducible Brillouin zone.[34]

The lifetimes predicted by both VC-NMD and Gamma-NMD show a ω^{-2} scaling at low frequency and a ω^{-4} scaling (for the alloys) and even faster for mid-range frequencies. The ω^{-2} scaling is due to three-phonon scattering processes [43, 72]. The ω^{-4} scaling is due to phonon-mass point defect scattering.[15, 41, 42, 44] A constant lifetime is observed at the highest frequencies for both VC-NMD and Gamma-NMD except at $c = 0.5$ for VC-NMD. We are not aware of any theoretical prediction of this high-frequency behavior.

The majority of the lifetimes predicted by both VC-NMD and Gamma-NMD are larger than the Ioffe-Regel (IR) limit, [2]

$$\tau_{IR} = \frac{2\pi}{\omega}. \quad (2.12)$$

The physical interpretation of the IR limit is a mode that scatters in a time equal to its oscillation period. Our results suggest that the IR limit is a good lower-limit for the lifetimes predicted by VC-NMD and Gamma-NMD for LJ argon (Fig. 2.4) and VC-NMD for SW silicon [see Fig. 2.8(a) in Section 2.5].

Overall, good agreement is seen in the predicted lifetimes from VC-NMD and Gamma-NMD in both magnitude and trends. The use of the VC normal modes is an approximation that becomes worse as the concentration is increased (see Appendix A.5), but our results suggest that the effect is only pronounced at the highest frequencies and at high alloy concentrations. The only approximation associated with Gamma-NMD is the use of the harmonic lattice dynamics-predicted frequencies and eigenvectors to map the atomic trajectories from the fully anharmonic MD simulations. This assumption has been shown to be valid for LJ argon below temperatures of 40 K.[68] Based on the good agreement with Gamma-NMD, the VC-NMD lifetimes are used along with the VC group velocities to predict thermal conductivity in Section 2.4. For Gamma-NMD, there is no accepted way to predict the mode group velocities, so that the thermal conductivity cannot be predicted using Eq. (2.1).

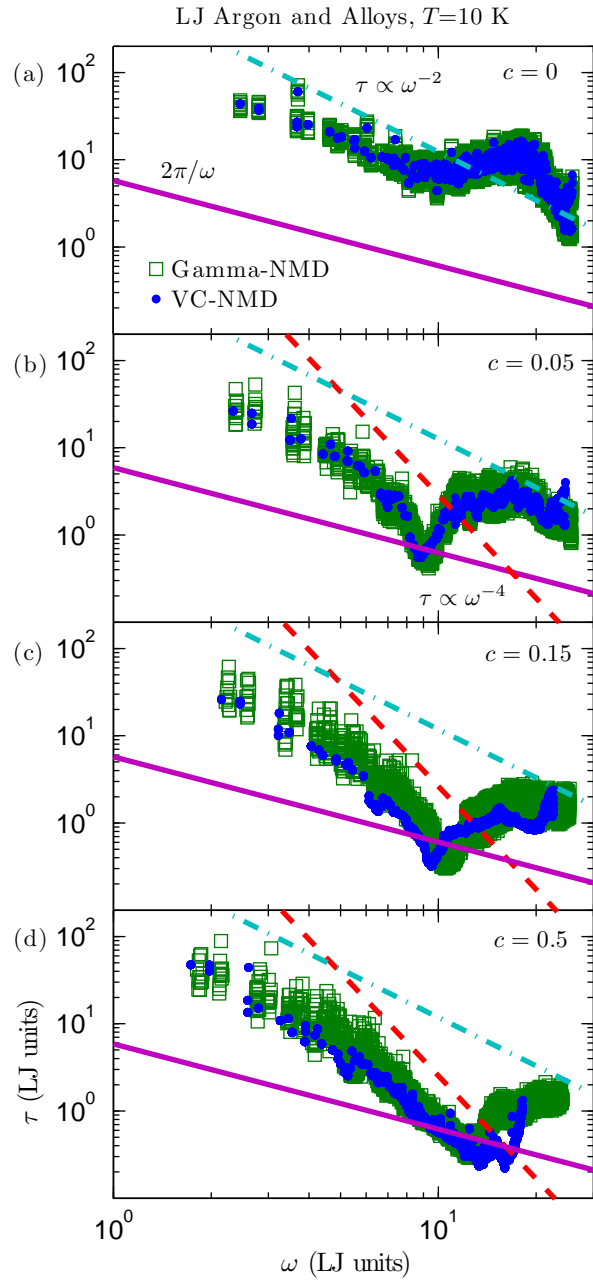


Figure 2.4: Lifetimes predicted using VC-NMD and Gamma-NMD from MD simulations of (a) perfect LJ argon and (b),(c),(d) mass-disordered LJ alloys for $N_0 = 10$. ω^{-2} and ω^{-4} scalings are observed at low to mid frequencies. For both VC-NMD and Gamma-NMD, most mode lifetimes are greater than the Ioffe-Regel limit of $2\pi/\omega$. [2] While there is more scatter in the Gamma-NMD data (see Section 2.3.3), the lifetime magnitudes and trends agree well, an important consideration when comparing the VC-NMD and VC-ALD lifetimes in Fig. 2.5(a).

From VC-ALD

Under the VC approximation, the ALD calculations[68] are performed on the conventional unit cells of LJ argon and SW silicon with a single atomic mass based on the alloy concentration. The ALD calculations scale as $b^4(N_0)^2$.[3] Disorder is not included explicitly but is treated using perturbation theory. Assuming phonon scattering mechanisms to operate independently, the effective phonon lifetime can be found using the Matthiessen rule, [19]

$$\frac{1}{\tau(\nu)} = \frac{1}{\tau_{p-p}(\nu)} + \frac{1}{\tau_{p-d}(\nu)}, \quad (2.13)$$

where $\tau_{p-p}(\nu)$ accounts for intrinsic phonon-phonon scattering and $\tau_{p-d}(\nu)$ accounts for phonon-defect scattering.

Phonon-phonon scattering in ALD is modeled by including three-phonon processes.[24, 26, 68] The present study is concerned with temperatures much less than the melting temperature of either LJ argon [53] or SW silicon[35] so that we believe the effects of higher-order phonon processes are negligible.[68, 73] We predict the phonon-phonon lifetimes using the method described in Ref. 68, with all classical expressions for the populations to remain consistent with the classical MD-based methods from Section 2.3.3.

Using perturbation theory, Tamura derived a general expression for phonon scattering by mass point defects to second order that was applied to study isotopic germanium.[15] By considering the symmetry properties of the FCC lattices considered in this work, his expression reduces to

$$\frac{1}{\tau_{p-d}(\nu)} = \frac{\pi}{2} g_2 \omega^2(\nu) DOS[\omega(\nu)], \quad (2.14)$$

where

$$g_n = \sum_{\mu} c^{\mu} (1 - m^{\mu}/\bar{m}^{\mu})^n. \quad (2.15)$$

Here, c^{μ} and m^{μ} are the concentration and mass of the μ -th species and \bar{m}^{μ} is the average mass. Bond disorder can be accounted for using a similar expression with an average atomic radius or suitable scattering cross-section. [41, 42] For the binary LJ argon and SW silicon alloys considered here, there is one atom type in the unit cell with $\mu = i, j$, so that the alloying atom labeled by m_c^j can be considered to be an “isotope” of the atom labeled m_{1-c}^i .

The lifetimes predicted by VC-ALD for LJ argon at a concentration of 0.05 are plotted in Fig. 2.5(a).[?] Also plotted are the lifetimes for the perfect system and from the VC-NMD predictions [Fig. 2.4(b)] at this concentration. At low frequencies, where the DOS is Debye-like [$D(\omega) \propto \omega^2$, Fig. 2.2], $\tau_{p-p}(\nu)$ scales as ω^{-2} , a scaling also observed in the VC-NMD and Gamma-NMD lifetimes. Under the Debye-approximation, the phonon scattering due to mass point-defects is predicted to scale as ω^{-4} from Eq. (2.14). [15, 44] This scaling is observed in the VC-NMD, Gamma-NMD, and VC-ALD predicted lifetimes in the mid-frequency range. VC-ALD does not predict the frequency-independent lifetimes at high frequency for LJ argon observed in VC-NMD and Gamma-NMD, and a significant number fall below the IR limit. The lifetimes predicted by NMD and ALD for the perfect LJ argon crystal agree within 20% on a

mode-by-mode basis, and the resulting thermal conductivities agree within their uncertainties (see Table A.1).

Tamura applied his theory to predict the reduction of lifetimes in isotopic germanium, which is weakly disordered ($\sim 5\%$ variation in the atomic masses). In the LJ alloys, the masses differ by a factor of three. Large mass ratios were also considered in DFT VC-ALD studies of SiGe (mass ratio of 2.6)[24], PbTeSe (2.6)[26], and MgSiSn (4.9)[29]. The importance of higher-order interactions in the Tamura theory can be estimated by the disorder strength (i.e., g_n for $n > 2$).[15] For isotopically-disordered germanium, Tamura estimated that the higher-order contributions were negligible ($g_2 = 5.87 \times 10^{-4}$, $g_3 \sim 10^{-7}$, and $g_4 \sim 10^{-7}$).[15] For LJ argon at a concentration of 0.15, $g_2 = 0.3018$, $g_3 = -0.3250$ and $g_4 = 0.4411$. It is possible that the neglect of the higher-order interactions in the Tamura theory is responsible for the discrepancy of the lifetimes predicted by VC-NMD and Gamma-NMD versus VC-ALD at high frequencies. Full evaluation of the higher-order interactions in the Tamura theory is of similar complexity to anharmonic phonon interaction, [68, 72, 73] and is beyond the scope of this work.

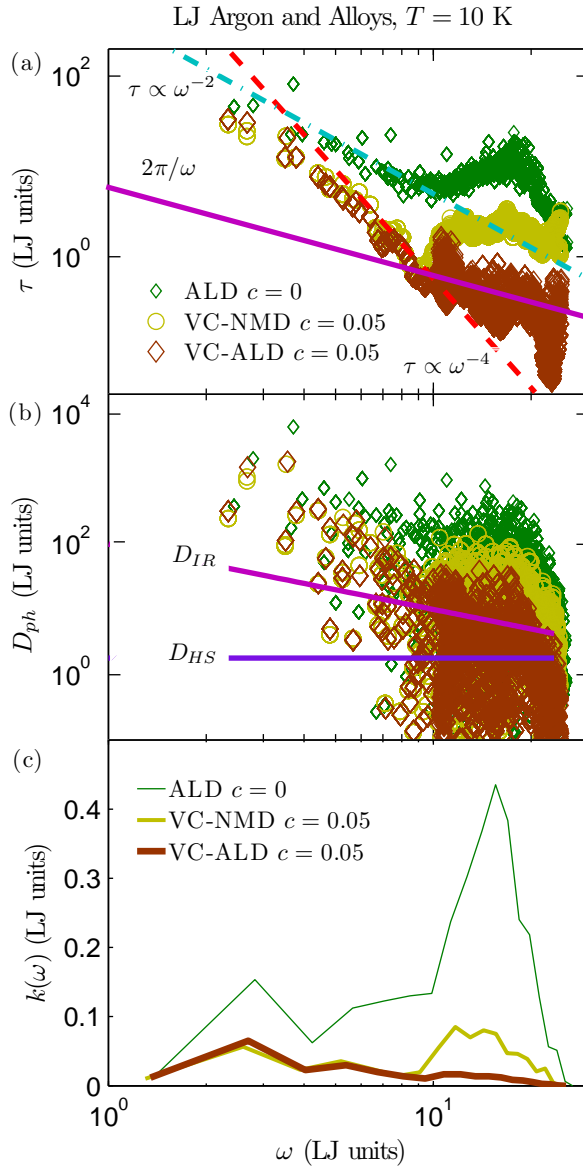


Figure 2.5: (a) Predicted lifetimes using VC-NMD and VC-ALD for LJ argon ($T = 10$ K, $N_0 = 10$, and $c = 0.05$). (b) Mode diffusivities compared to the high-scatter limit, D_{HS} [Eq. (2.18)], and IR limit, D_{IR} [Eq. (2.19)]. VC-NMD and VC-ALD predict a large number of high-frequency modes with $D_{ph} < D_{HS}$. (c) Thermal conductivity frequency spectrum, which peaks at high frequency, in contrast to SW silicon [(Fig. 2.8(c)]].

2.3.4 Diffusivities

We now use the AF theory to provide a lower limit for the contribution of a given vibrational mode to thermal conductivity. While studies have been performed on alloying the amorphous phase, [20] the AF theory has not been previously applied to disordered lattices. In the classical, harmonic limit for specific heat, a mode's contribution to the thermal conductivity of is determined by its diffusivity,

$$D_{ph,n}(\kappa) = v_{g,n}^2(\kappa) \tau(\kappa), \quad (2.16)$$

such that from Eq. (2.1)

$$k_{ph,n} = \sum_{\kappa} \sum_{\nu} \frac{k_B}{V} D_{ph,n}(\kappa). \quad (2.17)$$

The lower limit for phonon diffusivity is zero since the group velocities can be zero (e.g., optical modes at the Brillouin zone center).

In the high-scatter limit,[6] the diffusivity of each mode is

$$D_{HS} = \frac{1}{3} v_s a, \quad (2.18)$$

which leads to Eq. (2.3). The physical interpretation of Eq. (2.18) is that all vibrational modes transport heat at the sound speed and have a mean free path of the lattice spacing. Based on the IR limit, another possible lower-bound of diffusivity is

$$D_{IR} = \frac{2\pi}{3} \frac{v_s^2}{\omega}. \quad (2.19)$$

To evaluate Eqs. (2.18) and (2.19), the sound speed is estimated by

$$v_s = \frac{1}{3} v_{s,L} + \frac{2}{3} v_{s,T}, \quad (2.20)$$

where $v_{s,L}$ and $v_{s,T}$ are the longitudinal and transverse sound speeds calculated from the elastic constants, [57] which agree within 20% with the branch-averaged sound speeds along the high-symmetry dispersion directions [100],[110], and [111]. For LJ argon and SW silicon, $v_s = 6.93$ (LJ units) and 5,790 m/s. The Cahill-Pohl model assumes Eq. (2.19) for the mode diffusivities.[6] As seen in Fig. 2.5(b) for the LJ argon alloy at a concentration of 0.05, VC-NMD and VC-ALD predict [from Eq. (2.16), using the x -component of group velocity], a significant number of modes with $D_{ph}(\kappa)$ less than D_{HS} , and D_{IR} approaches D_{HS} at high frequencies. For both VC-NMD and VC-ALD, we approximate $\mathbf{v}_{g,n}(\kappa)$ from the VC dispersion (Section 2.3.2) so that any differences in diffusivity D_{ph} will come from the predicted lifetimes.

In a disordered system, modes can transport heat by harmonic coupling in the AF theory of diffusons.[39] While the high-scatter model assumes a mode-independent diffusivity, the AF theory is capable of predicting mode-specific thermal diffusivities D_{AF} . [20, 40, 74] Since the AF theory is harmonic, the diffusivities typically diverge as the frequency approaches zero because these vibrations are long-wavelength plane waves that are weakly scattered by the disorder. [75, 76] The mode-specific diffusivities, D_{AF} , of an LJ argon amorphous phase (see Section 2.2.3)[?] are plotted in Fig. 2.6 along with D_{HS} and D_{IR} . Except at the highest frequencies, the diffusivity

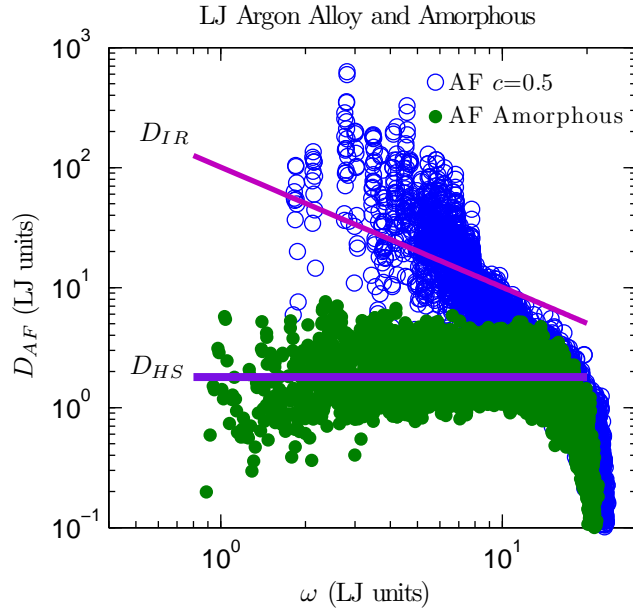


Figure 2.6: AF theory predictions of disordered mode diffusivities for LJ argon alloy and amorphous phases. The amorphous phase is well-described by a mode-independent diffusivity D_{HS} [Eq. (2.18)]. The system size for the alloy is $N_0 = 10$ (6,912 atoms), and the amorphous phase has 6,912 atoms.

of all amorphous modes can be approximated using the mode-independent diffusivity D_{HS} . The lower-limit D_{IR} is clearly an overprediction for the amorphous mode diffusivities. Also plotted in Fig. 2.6 are diffusivities predicted from the AF theory for the explicitly-disordered LJ argon lattice supercell alloy at a concentration of 0.5. As expected, the AF theory predictions diverge at low frequency.[?] The diffusivity of all modes are larger than D_{HS} except at the highest frequencies, where they tend to zero as with the amorphous phase. This result supports the hypothesis that the lower-bound of the VC predicted phonon diffusivity should be D_{HS} (and not zero as for a crystal), which is further explored in Sections 2.4 and 2.5.

2.3.5 Discussion

In this section, in anticipation of the thermal conductivity predictions in Section 2.4, we discuss two possible sources of error in the VC-predicted mode properties. To start, we note that for disordered systems, it is generally only possible to assign a unique lifetime and group velocity to vibrational modes in the low-frequency, propagating limit. [40, 77] The mode diffusivity is the fundamental transport property. [20, 39, 40]

We believe that the VC-predicted group velocities, particularly for $v_{g,n}(\kappa) \approx 0$, are an underprediction of the velocity scale required to evaluate Eq. (2.16). This statement is supported by the AF-theory diffusivities plotted in Fig. 2.6, which are finite for the majority of the frequency range the LJ alloy at a concentration of 0.5. While the diffusivity from Eq. (2.16) can be zero because of the VC predicted group velocities, this result is not consistent with the AF theory predictions.

The VC-NMD and Gamma-NMD predicted lifetimes are generally larger than the IR limit for LJ argon and its alloys (see Fig. 2.4). The constant lifetime observed at the highest frequencies for both VC-NMD (except at $c = 0.5$) and Gamma-NMD is consistent with the plateau of mode diffusivity at high frequency predicted for a model disordered lattice, which was explained by a plateau in the vibrational mode lifetimes. [78] Recently, a study of model disordered lattices predicted the mid-frequency minimum and the high-frequency plateau of the mode diffusivities.[?] Similar behavior of the mode diffusivities has been observed in model jammed systems.[76, 77] VC-ALD predicts essentially monotonically decreasing lifetimes with increasing frequency for the LJ argon alloys [Fig. 2.5(a)] with many falling below the IR limit. Because VC-NMD and VC-ALD use the same values for $v_{g,n}(\kappa)$, the mode diffusivities will therefore be underpredicted for VC-ALD compared to VC-NMD for the LJ argon alloys because of the lifetime underprediction.

2.4 Thermal Conductivity Prediction

The thermal conductivities of the LJ systems can now be predicted from Eq. (2.1) using the vibrational mode properties from VC-NMD and VC-ALD. Given the discussion regarding the VC-predicted mode properties in Section 2.3.5, we also predict thermal conductivity using the equilibrium MD-based GK method, which is a top-down method that does not make any approximations about the nature of the vibrational modes. Thermal conductivities predicted by the GK method naturally capture all scattering mechanisms. [4, 55, 79] The heat current was computed every ten time steps from the same atomic trajectories (positions and velocities) used for the VC-NMD and Gamma-NMD calculations. The thermal conductivity is determined from the maximum of the integral of the heat current autocorrelation function.

The thermal conductivities predicted by VC-NMD, VC-ALD, and GK are system size-dependent [i.e., $k = k(N_0)$] for all lattices and methods except perfect LJ argon from GK.[37] To predict a bulk thermal conductivity, k_{bulk} , a linear extrapolation procedure is used, whereby

$$\frac{k(N_0)}{k_{bulk}} = 1 - \frac{c_0}{N_0}, \quad (2.21)$$

where c_0 is a constant.[3, 27, 28] The thermal conductivity is predicted for varying system sizes and the bulk thermal conductivity is obtained by fitting Eq. (2.21) to the data. For VC-NMD and VC-ALD, the validity of Eq. (2.21) requires that the low-frequency modes be dominated by phonon-phonon scattering (i.e., $\tau \propto \omega^{-2}$) and follow the Debye approximation with respect to the group velocity and DOS. [27, 28] For the LJ argon alloys, this requirement is satisfied for modest system sizes (for $N_0 = 6$ to 12) so that both VC-NMD and VC-ALD thermal conductivity predictions can be extrapolated to a bulk value.

Bulk thermal conductivity predictions for the LJ argon alloys using VC-NMD, VC-ALD, and GK are tabulated in Table A.1 and plotted in Fig. 2.7. Also plotted in Fig. 2.7 is the high-scatter thermal conductivity prediction k_{HS} [Eq. (2.3)]. The thermal conductivity predicted for the LJ amorphous phase by GK is 0.17 W/m-K, which is in good agreement with k_{HS} (0.16 W/m-K) for the perfect crystal. The predicted thermal conductivities of the LJ argon alloys at high concentration are a factor of two to three larger than k_{HS} . While agreement between the three methods is found for the perfect crystal, VC-NMD and VC-ALD underpredict the alloy thermal conductivities compared to GK. The underprediction is modest for VC-NMD, where k_{NMD} is 80% of k_{GK} or greater for all concentrations. The VC-ALD method significantly underpredicts the thermal conductivity of the LJ argon alloys. The largest deviation is at a concentration of 0.05, where k_{VC-ALD} is 56% of k_{GK} .

In Section 2.3.4, we argued for the existence of a minimum mode diffusivity, D_{HS} [Eq. (2.18)]. As shown in Fig. 2.5(b), the diffusivities of many high-frequency modes in the LJ alloys, predicted by both VC-NMD and VC-ALD, fall below this limit. Based on this observation, we propose that any diffusivity below the limit be set to D_{HS} for thermal conductivity prediction. The results of this adjustment, referred to as VC-NMD* and VC-ALD*, are plotted in Fig. 2.7 and included in Table A.1. The adjusted thermal conductivities predicted by VC-NMD* are now within 10% of the GK value for all concentrations, which is within the prediction uncertainties. Combined with D_{HS} , we believe that the VC-NMD predicted diffusivities are good representations for the explicitly-disordered modes present in the MD simulations. Another possible adjustment, D_{IR} [Eq. (2.19)], results in a thermal conductivity of 0.94 ± 0.09 W/m-K for the LJ argon alloy at a concentration of 0.05, well above the value predicted by GK. We also note that the thermal conductivity of the amorphous phase is well-modeled by a mode-independent diffusivity D_{HS} , while D_{IR} overpredicts for all modes in the amorphous phase (see Fig. 2.6). Thus, we believe that D_{HS} is the more appropriate high-scatter limit.

By applying the high-scatter limit adjustment VC-ALD*, the thermal conductivities are brought into marginally better agreement with the GK values, worst for a concentration of 0.05, where k_{VC-ALD^*} is 65% of k_{GK} . As seen in Fig. 2.5(b), the VC-ALD method fails to accurately predict the high-frequency mode diffusivities for LJ argon alloys. Since the group velocities are the same for VC-NMD and VC-ALD, the underprediction of the high-frequency diffusivities is due to the underprediction of the high-frequency mode lifetimes from VC-ALD compared to VC-NMD. We know that the VC-NMD predicted lifetimes are more accurate values due to their agreement with Gamma-NMD [Fig. 2.4].

The thermal conductivity spectrum, defined as the contribution to thermal conductivity of modes at a given frequency, is plotted in Fig. 2.5(c) for VC-NMD and VC-ALD for the perfect crystal and the alloy with a concentration of 0.05. The thermal conductivity of LJ argon and its alloys has important contributions from high-frequency modes. VC-ALD underpredicts the

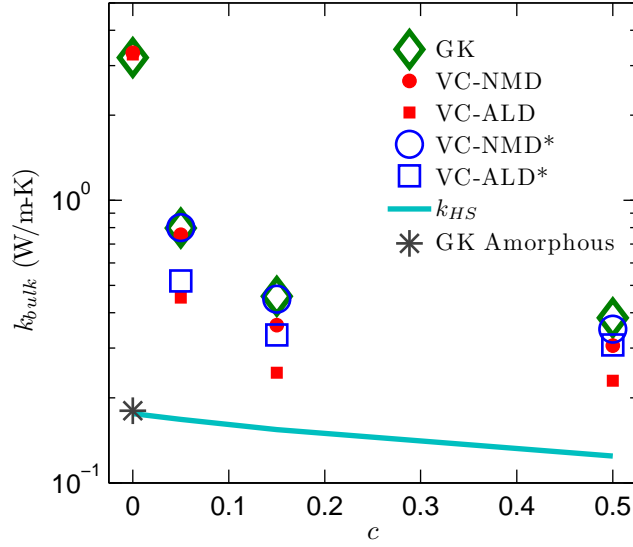
LJ Argon and Alloys, $T=10$ K

Figure 2.7: Thermal conductivity predictions for LJ argon and alloys at $T=10$ K using the VC-NMD, VC-ALD, and GK methods. The high-scatter thermal conductivity prediction k_{HS} [Eq. (2.3)] and the high-scatter adjusted VC-NMD* and VC-ALD* are also plotted.

high-frequency diffusivities compared to VC-NMD, which leads to an underprediction of the high-frequency thermal conductivity spectrum compared to VC-NMD. This result can be traced back to an underprediction of the high-frequency lifetimes compared to VC-NMD and Gamma-NMD [Fig. 2.5(a)].

Table 2.1: Thermal conductivity predictions using the VC-NMD, VC-ALD, and GK methods. For LJ argon alloys, the bulk extrapolation is used for all three methods. For SW silicon alloys, only VC-ALD and GK can be used to extrapolate a bulk thermal conductivity (see Section 2.4). For VC-NMD and GK, the uncertainties are estimated by omitting independent simulations from the ensemble averaging (see Section 2.2.3). For VC-ALD, the uncertainties are estimated by omitting extrapolation points used for Eq. (2.21).

c	GK	VC-NMD	VC-ALD	VC-NMD*	VC-ALD*	
LJ						
0.00	3.3 ± 0.1	3.3 ± 0.1	3.4 ± 0.1			
0.05	0.80 ± 0.07	0.76 ± 0.07	0.45 ± 0.02	0.80 ± 0.1	0.52 ± 0.05	
0.15	0.46 ± 0.07	0.36 ± 0.04	0.24 ± 0.01	0.45 ± 0.05	0.33 ± 0.07	
0.50	0.38 ± 0.07	0.31 ± 0.04	0.23 ± 0.01	0.35 ± 0.05	0.31 ± 0.07	
SW						
0.00	520 ± 30		480 ± 20			
0.05	20 ± 2		24 ± 2		24 ± 2	
0.15	9.9 ± 0.9		12 ± 1		12 ± 1	
0.50	9.3 ± 0.9		11 ± 1		11 ± 1	

2.5 SW silicon

The failure of VC-ALD to predict the thermal conductivities of the LJ alloys is due to an underprediction of the high-frequency mode lifetimes, which make an important contribution to the thermal conductivity [see Sections 2.3.4 and 2.4, Figs. 2.5(a) and 2.5(c)]. To provide a contrast, we now predict the vibrational mode properties and thermal conductivity for bulk and alloyed SW silicon, where it is known that low-frequency modes dominate the thermal conductivity. [56, 80] The lifetimes for the perfect crystal and an alloy with a concentration of 0.5 predicted by VC-NMD and VC-ALD are plotted in Fig. 2.8(a). The VC-NMD predicted lifetimes are generally larger than the IR limit for SW silicon alloys, similar to the VC-NMD predictions for the LJ argon alloys (Fig. 2.4). Unlike the LJ argon alloys, the VC-NMD and VC-ALD predicted lifetimes agree over most of the frequency spectrum, except at the highest frequencies, where VC-ALD underpredicts VC-NMD and falls below the IR limit. The high-frequency plateau of the VC-NMD predicted lifetimes for LJ argon (Fig. 2.4) is not seen for SW silicon. As seen in Figs. 2.5(b) and 2.8(b), VC-NMD and VC-ALD both predict a significant number of modes with $D_{ph}(\kappa)$ less than D_{HS} for both the LJ argon and SW silicon alloys.

The thermal conductivity spectra for bulk SW silicon and an alloy with a concentration of 0.5 are plotted in Fig. 2.8(c). For bulk and the alloy, the thermal conductivity is dominated by low-frequency modes, so that large system-sizes are needed to satisfy the extrapolation requirements and only GK and VC-ALD can be used to predict a bulk value from Eq. (2.21). While a previous study found that it was necessary to use cell sizes of $N_0 = 60$ for Tersoff silicon alloys,[71] we find that Eq. (2.21) is valid for SW silicon and $38 \leq N_0 \leq 42$. This system-size requirement highlights the efficiency of the VC-ALD method compared to VC-NMD, which is necessary when computationally-expensive DFT calculations are used. [16, 24, 26, 28, 81, 82] The bulk thermal conductivity predictions for VC-ALD and GK are shown in Table A.1 and plotted in Fig. 2.9. The alloy thermal conductivities predicted by VC-ALD are 20% larger than those from GK, in contrast to VC-ALD underpredicting for LJ argon alloys. This overprediction by VC-ALD compared to GK is close to the overprediction (15%) of VC-ALD using DFT calculations of SiGe alloys compared to experiment without including disorder explicitly.[24]

The predicted thermal conductivities for the SW silicon alloys at all concentrations are over an order of magnitude larger than the high-scatter prediction, k_{HS} . Because the thermal transport in SW silicon is dominated by low-frequency modes, the high-scatter adjustment VC-ALD* is within one percent compared to the unadjusted VC-ALD. While higher-order interactions in the Tamura theory may be responsible for the discrepancy of the lifetimes predicted by VC-NMD and VC-ALD in SW silicon at the highest frequencies [Fig. 2.8(a)], this effect is not important to the overall thermal transport. VC-ALD predicts accurate alloy thermal conductivities for SW silicon because it is a low-frequency dominated material, which is the frequency range where the standard application of the Tamura theory is valid.[15]

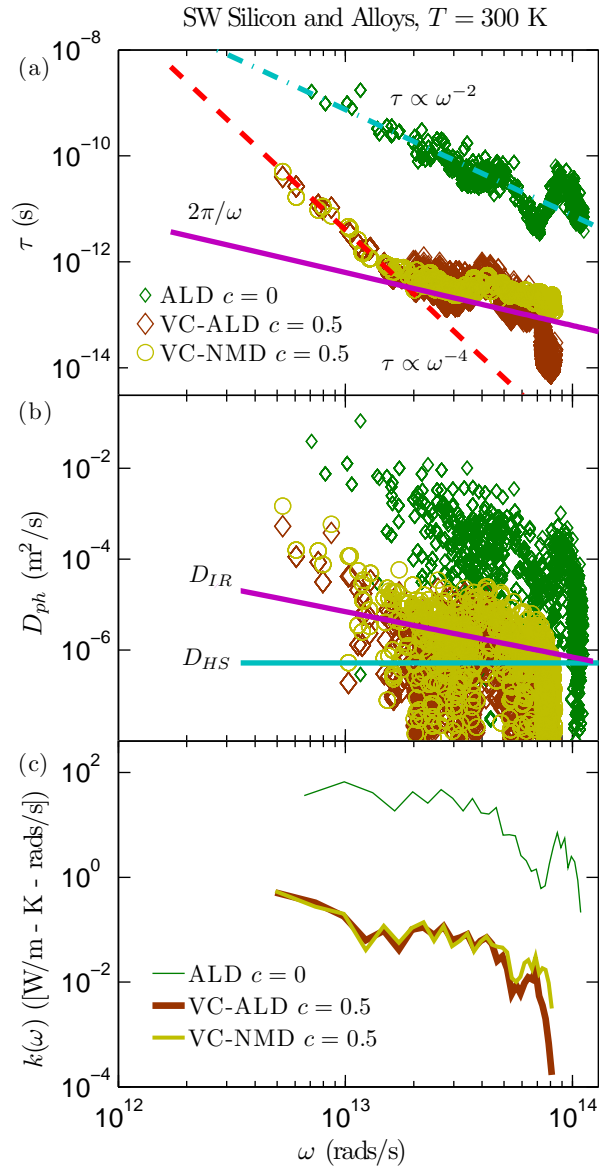


Figure 2.8: (a) Predicted lifetimes using VC-NMD and VC-ALD for SW silicon ($T = 300$ K, $N_0 = 8$, and $c = 0.05$). (b) Mode diffusivities compared to the high-scatter limit, D_{HS} [Eq. (2.18)], and the IR limit, D_{IR} [Eq. (2.19)]. VC-NMD and VC-ALD predict a large number of high-frequency modes with $D_{ph} < D_{HS}$, as seen in the LJ argon alloys [Fig. 2.5(b)]. (c) Thermal conductivity frequency spectra, which peak at low frequency, in contrast to LJ argon [Fig. 2.5(c)].

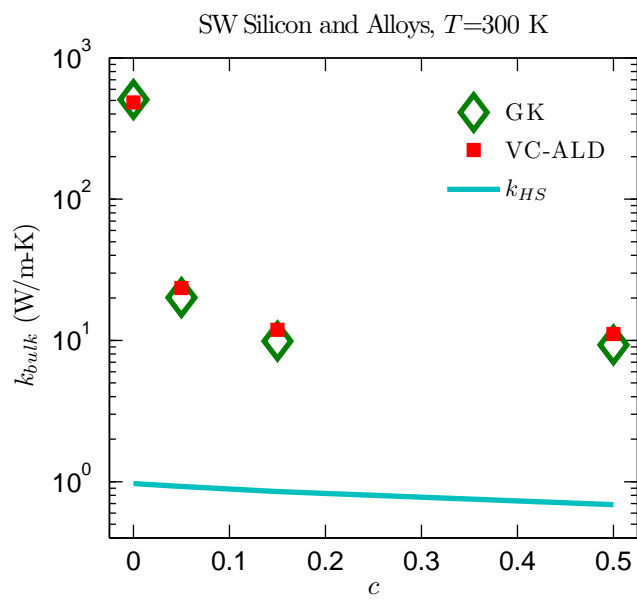


Figure 2.9: Thermal conductivity predictions for SW silicon and alloys at a temperature of 300 K using the VC-ALD and GK methods. The high-scatter thermal conductivity prediction k_{HS} is also plotted. The adjusted VC-ALD* is not shown since it differs by less than one percent compared to VC-ALD.

2.6 Summary

In this study, we investigated the use of the VC approximation for predicting the vibrational mode properties and thermal conductivity of LJ argon and SW silicon alloys by a detailed comparison of the VC-NMD, VC-ALD, and GK methods. By using computationally-inexpensive empirical potentials we self-consistently studied the effects of disorder both explicitly (Sections 2.3.1, 2.3.2, 2.3.3, 2.3.4, and 2.5) and as a perturbation (Sections 2.3.3 and 2.5). By spanning a range of disorder, the limits of the perturbative models were examined. A breakdown of the VC-ALD method was identified for LJ argon alloys by a comparison with the VC-NMD method in Section 2.3.3 and a correction was suggested in Section 2.4. The mode properties and thermal conductivity of the SW silicon alloys were predicted in Section 2.5 and provided a contrast to the LJ argon alloys, which have a different thermal conductivity spectrum.

The results for the SW silicon and LJ argon alloys suggest that modeling of thermal transport in ordered and disordered lattices can be separated into two broad groups: low-frequency dominated and full-spectrum materials. Materials dominated by low-frequency modes tend to have high thermal conductivities that are significantly larger than the high-scatter limit [Eq. (2.3)], which is due to the large group velocities and long lifetimes of low-frequency modes.[16, 17, 18, 24, 45, 46, 47, 83] These low-frequency modes closely follow the scalings predicted by the perturbative VC-ALD models, which are valid at low-frequencies.

LJ argon is a material whose thermal transport has significant contribution from high-frequency modes, even for the bulk [see Fig. 2.5 (c)]. This high-frequency range is where we predict that the perturbative Tamura theory will have non-negligible contributions from higher-order interactions (see Section 2.3.3). While the higher-order interactions in the Tamura theory are also predicted to be non-negligible for SW silicon, this does not affect the thermal conductivity predictions significantly because high-frequency modes are not important to thermal transport. The negligible contributions of high-frequency modes is demonstrated by experimental measurements of the thermal conductivity of SiGe alloys, which exceed the high-scatter limit by more than an order of magnitude at room temperature for all compositions. [6, 46, 47, 83] Experimentally-accurate theoretical predictions[24] also demonstrate that high-frequency modes are unimportant to thermal transport, although they do serve as important scattering channels. [23]

The VC-ALD method provides a computationally inexpensive framework, which is essential when using *ab initio* methods for predicting thermal conductivity. [16, 23, 24, 25, 26, 27, 28, 29, 30] Based on our results, we believe that the Tamura theory breaks down for mode diffusivities predicted to be below the high-scatter limit, D_{HS} [Eq. (2.18)]. This breakdown may be true for the high-frequency modes of any disordered lattice[78] and the high-scatter limit D_{HS} should be considered whenever the perturbative VC-ALD method is used. Although the high-scatter limit of diffusivity is usually interpreted as a minimum mean free path, [5, 6, 78, 84] we find that this concept is not necessary for interpreting the results of this work. In a disordered lattice, the fundamental quantities are the mode lifetime and diffusivity[2, 21, 39, 76, 77, 78?] and the VC predicted group velocity is an approximation.

This work was supported by AFOSR award FA95501010098 and by a grant of computer time from the DOD High Performance Computing Modernization Program at the US Army Engineer Research and Development Center. We thank Davide Donadio, Jivtesh Garg, Asad Hasan, Ankit Jain, Craig Maloney, and Zhiting Tian for helpful discussions.

July 24, 2013
DRAFT

Chapter 3

Vibrational Mean Free Paths and Thermal Conductivity Accumulation Functions for Amorphous Materials

test

3.1 new section

July 24, 2013
DRAFT

Chapter 4

Origin of the Exceptionall Low Thermal Conductivity of PCBM Thin Films

test

4.1 new section

July 24, 2013
DRAFT

Chapter 5

Conclusion

There are two sections to this introductory chapter.

5.1 new section

test section

July 24, 2013
DRAFT

Appendix A

Vibrational Lifetimes from Molecular Dynamics

Two frequency-domain methods for predicting phonon frequencies and lifetimes using the phonon spectral energy density are described. Both methods draw input from molecular dynamics simulations and lattice dynamics calculations, but differ in the form of the phonon spectral energy density. One phonon spectral energy density expression (referred to as Φ) can be formally derived from lattice dynamics theory. A similar approach in the time domain has been validated [Turney et al. *Phys. Rev. B* **79**, 224305 (2009)]. The other phonon spectral energy density expression (referred to as Φ') has been proposed [Thomas et al., *Phys. Rev. B* **81**, 081411(R) (2010)] but not validated. The expressions for Φ and Φ' are presented and then applied to predict the phonon properties and thermal conductivities of three systems: Lennard-Jones argon, Stillinger-Weber silicon, and a carbon nanotube modeled using the Reactive Empirical Bond Order potential. Φ' does not capture the total phonon spectral energy density predicted by Φ and therefore cannot correctly predict the phonon lifetimes or thermal conductivity. Its use in future work is discouraged and we recommend the use of Φ .

A.1 Introduction

Phonons are the dominant carriers of thermal energy in dielectric and semiconducting crystals [70, 85, 86, 87, 88?]. While substantial effort has been devoted to developing theories of phonon transport, the current understanding is incomplete, even in bulk materials. For example, which phonon modes dominate thermal energy transport and the importance of interactions involving four or more phonons are still being investigated [22, 28, 85, 87, 88]. The situation becomes more complicated in nanostructures, where the phonons also interact with free surfaces and interfaces [4, 49, 79, 89, 90, 91, 92, 93, 94, 95, 96, 97?].

Analytical models of thermal transport, such as the Debye model, are limited by the necessary approximations and assumptions [43, 98, 99]. With the Green-Kubo or non-equilibrium direct methods, molecular dynamics (MD) simulations can be used to predict thermal conductivity, but only in a classical (i.e., high-temperature) framework [3, 28, 37, 67, 79, 80, 100]. Because the analysis in these two MD-based methods is performed at the system level, no information about

the phonons is obtained. Phonon specific heats, group velocities, and lifetimes are the required inputs for predicting thermal conductivity at the phonon-mode-level using Boltzmann transport equation-based models [3, 4, 28, 37, 67, 80, 99]. These phonon properties can be predicted using harmonic and anharmonic lattice dynamics calculations [3, 67, 70, 72, 88?], where quantum statistical effects can be naturally included. Anharmonic lattice dynamics calculations are limited to three-phonon scattering events, however, and are thus only valid at low temperatures [3, 28, 87, 88].

At high temperature, four-phonon and higher-order processes become important to thermal transport [3, 28, 87, 88]. All orders of phonon processes are present in a MD simulation as the positions and momenta of the atoms are evolved using the full anharmonicity of the interatomic interactions [28, 37]. Phonon properties can be predicted from a MD simulation using normal mode analysis in the time domain [3, 4, 37, 38, 67, 101]. In Section A.2.1, we will describe how this approach can be performed in the frequency-domain using the phonon spectral energy density (SED, referred to as Φ). An alternative expression for the phonon SED (referred to as Φ'), was recently proposed but has not been rigorously tested [102, 103, 104]. Φ' was first used to predict the phonon dispersion curves of carbon nanotubes (CNTs) [102]. Thomas et al. used Φ' to predict the phonon lifetimes and thermal conductivity of isolated and water-filled CNTs, obtaining good agreement with other atomistic predictions [104]. The phonon lifetime reductions speculated for water-filled CNTs [104] and CNTs on SiO_2 substrates [105] suggest that Φ' captures phonon physics at least qualitatively. The phonon lifetimes and thermal conductivity for PbTe [106] and Half Heusler alloys [27] have also been predicted using Φ' . De Koker predicted the phonon lifetimes and thermal conductivity for MgO using an expression similar to Φ' (but different than Φ) [?]. Another recent atomistic study using Stillinger-Weber silicon predicted phonon lifetimes using both Φ and Φ' , but a detailed comparison of the predictions between the two was not performed [107].

The objective of this work is to assess the validity of Φ' as a phonon SED by comparing the phonon properties it predicts to those predicted by Φ . In Section A.2.1, we present the correct phonon SED (Φ), which requires the phonon mode eigenvectors. The expression for Φ is well-defined theoretically and has been tested and validated in previous studies in the time domain [3, 67]. In Section A.3.1, we present the proposed alternative expression for the phonon SED, Φ' , which does not require the phonon mode eigenvector [104]. Phonon frequencies, lifetimes, and thermal conductivities are then predicted and compared using Φ and Φ' for three test systems: Lennard-Jones (LJ) argon [34] in Section A.8.1, Stillinger-Weber (SW) silicon [35] in Section A.8.2, and an (8,8) CNT modeled with the reactive empirical bond order (REBO) potential [?] in Section A.8.3. While Φ' is found to accurately predict the phonon frequencies, we find that it does not correctly predict the phonon lifetimes because it does not capture the total phonon spectral energy density.

A.2 Phonon Spectral Energy Density

A.2.1 As Derived from Normal Mode Coordinates, Φ

The correct expression for the phonon SED, Φ , can be derived from the formulation of anharmonic lattice dynamics theory [70, 87, 88?]. As shown in Appendix (REF), the phonon SED at wavevector κ is a function of frequency, ω , and is given by

$$\Phi(\kappa, \omega) = \sum_{\nu}^{3n} C_0(\nu) \frac{\Gamma(\nu) / \pi}{[\omega_0(\nu) - \omega]^2 + \Gamma^2(\nu)}, \quad (\text{A.1})$$

which is a superposition of $3n$ Lorentzian functions with centers at $\omega_0(\nu)$ and linewidths $\Gamma(\nu)$ (one for each polarization, ν). The $C_0(\nu)$ terms are mode-dependent constants. For simplicity, we refer to $\Phi(\kappa, \omega)$ as Φ . The phonon kinetic energy normal mode coordinate, $\dot{q}(\nu; t)$, is [70]

$$\dot{q}(\nu; t) = 00 \sum_{\alpha, b, l}^{3n, N} 01 \sum_{\alpha, b}^{3n, N, 3n} \sqrt{\frac{m_b}{N}} \dot{u}_{\alpha}(b; t) e^*(\nu \alpha) \exp[i\kappa \cdot \mathbf{r}_0(lal)], \quad (\text{A.2})$$

where $e(\nu \alpha)$ are the components of the time-independent phonon mode eigenvector (see Section A.6.3), n is the number of atoms in the unit cell, m_b is the mass of the b^{th} atom in the unit cell and $\mathbf{r}_0(lal)$ is the equilibrium position vector of the l^{th} unit cell. There are N total unit cells and $\dot{u}_{\alpha}(b; t)$ is the α -component of the velocity of the b^{th} atom in the l^{th} unit cell at time t .

Given a set of atomic velocities from MD simulation and the phonon mode eigenvector, Φ can be calculated using

$$\Phi(\kappa, \omega) = 2 \sum_{\nu}^{3n} T(\nu; \omega) = 2 \sum_{\nu}^{3n} \lim_{\tau_0 \rightarrow \infty} \frac{1}{2\tau_0} \left| \frac{1}{\sqrt{2\pi}} \int_0^{\tau_0} \dot{q}(\nu; t) \exp(-i\omega t) dt \right|^2, \quad (\text{A.3})$$

and then fit using Equation (A.11) to extract the phonon properties $\omega_0(\nu)$ and $\Gamma(\nu)$.

The phonon lifetime, $\tau(\nu)$, is defined as $1/[2\Gamma(\nu)]$. In practice, τ_0 should be much larger than the longest phonon lifetime and the continuous fourier transform in Equation (A.23) is performed using a discrete fast fourier transform (see Section A.8.1, A.8.2 and A.8.3).

Previous work using normal mode analysis has represented the phonon energy in the time domain [3, 4, 37, 38, 67, 101], while Φ is a representation of the phonon energy in the frequency domain. The time- and frequency-domain approaches are mathematically equivalent by use of the Wiener-Khinchin theorem [27, 108]. The frequency-domain approach has the advantage of predicting both the phonon lifetime and frequency by fitting a simpler function than is required in the time-domain approach.

A.2.2 Derivation of Phonon Spectral Energy Density, Φ

(WORK)

To derive the correct expression for the phonon SED, Φ , we begin with harmonic lattice dynamics theory.[70, 88] The derivation outlined here is presented in detail in Appendix A.3.

In reciprocal space, the system Hamiltonian, H , is

$$\begin{aligned} H &= \frac{1}{2} \sum_{\alpha,b,l}^{3,n,N} 1 \sum_{\alpha,b}^{3,n} \sum_{\kappa,\nu}^{N,3n} [\dot{q}^*(\kappa; t) \dot{q}(\kappa; t) + \omega_0^2(\kappa) q^*(\kappa; t) q(\kappa; t)] \\ &= 0 \sum_{\alpha,b,l}^{3,n,N} 1 \sum_{\alpha,b}^{3,n} \sum_{\kappa,\nu}^{N,3n} [T(\kappa; t) + V(\kappa; t)], \end{aligned} \quad (\text{A.4})$$

where t is time, $\omega_0(\kappa)$ is the frequency of the phonon mode denoted by wave vector κ and dispersion branch ν , and N and n are the total number of unit cells and the number of atoms in the unit cell. The Hamiltonian is the total system energy and is the sum of the mode- and time-dependent kinetic and potential energies, $T(\kappa; t)$ and $V(\kappa; t)$. The phonon normal mode coordinate, $q(\kappa; t)$ and its time derivative, $\dot{q}(\kappa; t)$, are given by

$$q(\kappa; t) = 0 \sum_{\alpha,b,l}^{3,n,N} 01 \sum_{\alpha,b}^{3,n} \sum_{\kappa,\nu}^{N,3n} \sqrt{\frac{m_b}{N}} u_\alpha(l; t) e^*(\kappa \alpha) \exp[i\kappa \cdot \mathbf{r}_0(lal)] \quad (\text{A.5})$$

and

$$\dot{q}(\kappa; t) = 0 \sum_{\alpha,b,l}^{3,n,N} 01 \sum_{\alpha,b}^{3,n} \sum_{\kappa,\nu}^{N,3n} \sqrt{\frac{m_b}{N}} \dot{u}_\alpha(l; t) e^*(\kappa \alpha) \exp[i\kappa \cdot \mathbf{r}_0(lal)], \quad (\text{A.6})$$

where m_b is the mass of the b^{th} atom in the unit cell and $\mathbf{r}_0(lal)$ is the equilibrium position vector of the l^{th} unit cell. The α -component of the displacement from equilibrium, $u_\alpha(l; t)$, and velocity, $\dot{u}_\alpha(l; t)$, of the b^{th} atom in the l^{th} unit cell are time-dependent and are related to the phonon mode coordinates through the time-independent eigenvector that has components $e(\kappa \alpha)$.

The expectation value of the kinetic energy of each normal mode in the time domain is

$$\langle T(\kappa) \rangle = \lim_{\tau_0 \rightarrow \infty} \frac{1}{2\tau_0} \int_0^{\tau_0} \dot{q}^*(\kappa; t) \dot{q}(\kappa; t) dt. \quad (\text{A.7})$$

The expectation value of the kinetic energy of the normal mode can be transformed from the time domain to the frequency domain by Parseval's theorem,[108]

$$T(\kappa; \omega) = \lim_{\tau_0 \rightarrow \infty} \frac{1}{2\tau_0} \left| \frac{1}{\sqrt{2\pi}} \int_0^{\tau_0} \dot{q}(\kappa; t) \exp(-i\omega t) dt \right|^2. \quad (\text{A.8})$$

Starting from Eq. (A.8) and following the derivation in Appendix A.3, one arrives at the expression for the SED of a single phonon mode,

$$T(\kappa; \omega) = \frac{C_0(\kappa)}{2} \frac{\Gamma(\kappa)/\pi}{[\omega_0(\kappa) - \omega]^2 + \Gamma^2(\kappa)}, \quad (\text{A.9})$$

which is a Lorentzian function with center at $\omega_0(\kappa)$ and a half-width at half-maximum (linewidth) of $\Gamma(\kappa)$. The constant $C_0(\kappa)$ is defined in Eq. (A.24) in Appendix A.3. We know from anharmonic

lattice dynamics theory that the phonon linewidth is related to the phonon lifetime, $\tau(\nu)$, by[67, 72]

$$\tau(\nu) = \frac{1}{2\Gamma(\nu)}. \quad (\text{A.10})$$

The MD simulations we perform here are classical. For a classical system in the harmonic limit (i.e., temperature approaching zero) there is an equipartition of energy and $\sum_{\nu}^{3n} T(\nu; \omega) = \sum_{\nu}^{3n} V(\nu; \omega)$.[36] In an anharmonic system (i.e., a MD simulation), the assumption of equipartition of energy can be tested by predicting the system-level specific heat (see Section A.6.4). By assuming equipartition of energy, the phonon SED at a particular wavevector is

$$\Phi(\kappa, \omega) = 2 \sum_{\nu}^{3n} T(\nu; \omega) = \sum_{\nu}^{3n} C_0(\nu) \frac{\Gamma(\nu)/\pi}{[\omega_0(\nu) - \omega]^2 + \Gamma^2(\nu)}, \quad (\text{A.11})$$

which is a superposition of $3n$ Lorentzian functions with centers at $\omega_0(\nu)$ (one for each polarization). For simplicity, we refer to $\Phi(\kappa, \omega)$ as Φ . Given a set of atomic velocities, Φ can be calculated using Eq. (A.6) and (A.8), and then fit using Eq. (A.11) to extract the phonon properties $\omega_0(\nu)$ and $\tau(\nu)$.

Previous work using normal mode analysis has represented the phonon energy in the time domain, [3, 4, 37, 38, 67, 101] while Φ is a representation of the phonon energy in the frequency domain. The time- and frequency-domain approaches are mathematically equivalent by use of the Wiener-Khinchin theorem. [27, 108] The frequency-domain approach has the advantage of predicting both the phonon lifetime and frequency by fitting a simpler function than required in the time-domain approach.

(WORK)

We start from Eq. (A.6) and follow the formulation of anharmonic lattice dynamics theory. [70, 87, 88?] In an anharmonic system, the phonon populations fluctuate about the equilibrium distribution function.[88] The phonon mode coordinate for the mode described by (κ, ν) and its time derivative can be written as

$$q(\nu; t) = q_{SS}(\nu; t) + q_T(\nu; t) \quad (\text{A.12})$$

and

$$\dot{q}(\nu; t) = \dot{q}_{SS}(\nu; t) + \dot{q}_T(\nu; t). \quad (\text{A.13})$$

The steady-state (SS) and transient (T) parts and their time derivatives are given by

$$\begin{aligned} q_{SS}(\nu; t) &= C_1(\nu) \exp[i\omega_0(\nu)t] \\ &\quad + C_2(\nu) \exp[-i\omega_0(\nu)t], \end{aligned} \quad (\text{A.14})$$

$$\begin{aligned} q_T(\nu; t) &= \exp[-\Gamma(\nu)|t|] \{C_3(\nu) \exp[i\omega_0(\nu)t] \\ &\quad - C_4(\nu) \exp[-i\omega_0(\nu)t]\}, \end{aligned} \quad (\text{A.15})$$

$$\dot{q}_{SS}(\nu; t) = i\omega_0 \{C_1(\nu) \exp[i\omega_0(\nu)t] - C_2(\nu) \exp[-i\omega_0(\nu)t]\}, \quad (\text{A.16})$$

and

$$\begin{aligned}\dot{q}_T(\kappa; t) = & \exp[-\Gamma(\nu) |t|] \{ C_3(\nu) [i\omega_0(\nu) - \Gamma(\nu)] \exp[i\omega_0(\nu) t] \\ & - C_4(\nu) [i\omega_0(\nu) + \Gamma(\nu)] \exp[-i\omega_0(\nu) t] \},\end{aligned}\quad (\text{A.17})$$

where the C s are constants and $\omega_0(\nu)$ and $\Gamma(\nu)$ are the phonon mode frequency and linewidth. The transient part describes the creation of an excess in the population of a phonon mode for $t < 0$ and its decay back to equilibrium for $t > 0$.

Phonon population fluctuations are commonly modeled using the excitation and decay of a single phonon mode (i.e., the single mode relaxation time approximation). In a real system, there will be multiple phonons in each mode that simultaneously grow or decay with time. Thus, dealing only with \dot{q} , we let

$$\begin{aligned}\dot{q}(\kappa; t) = & \sum_j i \exp[-\Gamma(\nu) |t - t_j|] \times \\ & \{ A_j(\nu) [\omega_0(\nu) + i\Gamma(\nu)] \exp[i\omega_0(\nu) (t - t_j)] \\ & - B_j(\nu) [\omega_0(\nu) - i\Gamma(\nu)] \exp[-i\omega_0(\nu) (t - t_j)] \},\end{aligned}\quad (\text{A.18})$$

where many phonons in each mode, indexed by j , are simultaneously being created and destroyed. The phonons grow for $t < t_j$, decay for $t > t_j$, and A_j and B_j are constants. We are not concerned with the values of t_j , A_j , and B_j , though they should satisfy the long-time average $\langle \dot{q}^*(\nu; t) \dot{q}(\nu; t) \rangle = \langle \dot{q}_{SS}^*(\nu; t) \dot{q}_{SS}(\nu; t) \rangle$.

The expectation value of the kinetic energy of the normal mode in the time domain is

$$\langle T(\nu) \rangle = \frac{1}{2} \lim_{\tau_0 \rightarrow \infty} \frac{1}{\tau_0} \int_0^{\tau_0} \dot{q}^*(\nu; t) \dot{q}(\nu; t) dt. \quad (\text{A.19})$$

The expectation value of the kinetic energy of the normal mode can be transformed from the time domain to the frequency domain by Parseval's theorem,[108] giving

$$T(\nu; \omega) = \lim_{\tau_0 \rightarrow \infty} \frac{1}{2\tau_0} \left| \frac{1}{\sqrt{2\pi}} \int_0^{\tau_0} \dot{q}(\nu; t) \exp(-i\omega t) dt \right|^2. \quad (\text{A.20})$$

By substituting Eq. (A.18) into Eq. (A.20) and performing the time integration we find

$$\begin{aligned}T(\nu; \omega) = & \frac{1}{16\pi\tau_0} \left| \sum_j \exp[-i\omega t_j] \left\{ A_j(\nu) \frac{\omega_0(\nu) + i\Gamma(\nu)}{\omega_0(\nu) - \omega + i\Gamma(\nu)} \right. \right. \\ & \left. \left. + B_j(\nu) \frac{\omega_0(\nu) - i\Gamma(\nu)}{\omega_0(\nu) + \omega - i\Gamma(\nu)} \right\} \right|^2.\end{aligned}\quad (\text{A.21})$$

We are primarily interested in values of ω where $\omega \approx \omega_0$ when $\Gamma \ll \omega_0$ (this condition is met for the three systems studied here). When $\omega \approx \omega_0$, the term involving A_j becomes large and the term involving B_j can be neglected (alternatively, we could ignore the term involving A_j when $\omega \approx -\omega_0$). Hence, we find

$$\begin{aligned}T(\nu; \omega) = & \frac{1}{16\pi\tau_0} \sum_j \sum_{j'} \cos[\omega(t_{j'} - t_j)] A_j(\nu) A_{j'}(\nu) \\ & \times \frac{\omega_0^2(\nu) + \Gamma^2(\nu)}{\Gamma(\nu)} \frac{\Gamma(\nu)}{[\omega_0(\nu) - \omega]^2 + \Gamma^2(\nu)}.\end{aligned}\quad (\text{A.22})$$

We arrive at the expression for the phonon spectral energy density for the wavevector κ by summing Eq. (A.22) over the different polarizations ν ,

$$\Phi(\kappa, \omega) = 2 \sum_{\nu}^{3n} T(\nu; \omega) = \sum_{\nu}^{3n} C_0(\nu) \frac{\Gamma(\nu) / \pi}{[\omega_0(\nu) - \omega]^2 + \Gamma^2(\nu)}, \quad (\text{A.23})$$

where the factor of two comes from equipartition of kinetic and potential energy (valid for a harmonic classical system, see Section A.6.4), and

$$C_0(\nu) = \sum_j \sum_{j'} \cos [\omega(t_{j'} - t_j)] A_j(\nu) A_{j'}(\nu) \frac{\omega_0^2(\nu) + \Gamma^2(\nu)}{8\tau_0 \Gamma(\nu)}. \quad (\text{A.24})$$

Thus, the phonon spectral energy density $\Phi(\kappa, \omega)$ is a superposition of $3n$ Lorentzian functions with centers at $\omega_0(\nu)$ (one for each polarization) with a linewidth (half-width at half-maximum) of $\Gamma(\nu)$. Φ is a spectral energy density since its integral over all wavevectors and frequencies is the total crystal energy, i.e., the Hamiltonian is

$$H = \int_{V_{BZ}} \int_0^{\infty} \Phi(\kappa, \omega) d\omega d\kappa, \quad (\text{A.25})$$

where V_{BZ} is the volume of the first Brillouin zone. Like the frequency broadening, there is also a broadening of the SED in wavevector. [?] For a finite sampling of the first Brillouin zone, the Hamiltonian can be approximated by

$$H \approx 2 \sum_{\kappa, \nu}^{N, 3n} \langle T(\nu; t) \rangle = \sum_{\kappa}^N \int_0^{\infty} \Phi(\omega, \kappa) d\omega. \quad (\text{A.26})$$

A.2.3 Alternative Formulation, Φ'

We now seek to motivate the expression Φ' that was proposed in previous studies but has not been validated [102, 103, 104]. Thomas et al. [104] define

$$\Phi'(\kappa, \omega) = \frac{1}{4\pi\tau_0} \sum_{\alpha}^3 \sum_b^n \frac{m_b}{N} \left| \sum_l^N \int_0^{\tau_0} \dot{u}_{\alpha}(l; t) \exp[\Theta] dt \right|^2, \quad (\text{A.27})$$

where $\Theta \equiv i[\kappa \cdot \mathbf{r}_0(lal) - \omega t]$. To understand this expression, we start with the real-space atomic velocities as represented by the normal mode velocities, $\dot{q}(\kappa'; t)$ [70],

$$\dot{u}_{\alpha}(l; t) = 20 \sum_{\alpha, b, l}^{3, n, N} 21 \sum_{\alpha, b}^{3, n} \sum_{\kappa', \nu}^{N, 3n} \frac{1}{\sqrt{m_b N}} \exp[i\kappa' \cdot \mathbf{r}_0(lal)] e^*(\kappa' \cdot b) \dot{q}(\kappa'; t). \quad (\text{A.28})$$

Fourier transforming both sides of Equation (A.28) in time and space, taking the complex modulus, and summing over the atoms in the unit cell and the Cartesian directions yields

$$\begin{aligned} \lim_{\tau_0 \rightarrow \infty} \frac{1}{4\pi\tau_0} \sum_{\alpha}^3 \sum_b^n \frac{m_b}{N} \left| \sum_l^N \int_0^{\tau_0} \dot{u}_{\alpha}(l; t) \exp[\Theta] dt \right|^2 = \\ \lim_{\tau_0 \rightarrow \infty} \frac{1}{4\pi\tau_0} \sum_{\alpha}^3 \sum_b^n \left| \frac{m_b^{3/2}}{\sqrt{N}} \sum_l^N \sum_{\nu}^{3n} e^{*(\kappa_b)} \int_0^{\tau_0} \dot{q}(\kappa_{\nu}; t) \exp[\Theta] dt \right|^2, \quad (\text{A.29}) \end{aligned}$$

where the the sum over κ' on the right-hand-side is reduced to a single wavevector by the orthogonality of the allowed wavevectors over the periodic domain. Equation (A.27) is the finite integration of the left-hand-side of Equation (A.29). For simplicity, we refer to $\Phi'(\kappa, \omega)$ as Φ' . Given a set of atomic velocities, Thomas et al. extract the phonon properties $\omega_0(\kappa)$ and $\tau(\kappa)$ from Equation (A.27) by fitting Φ' for a given wavevector to a superposition of Lorentzian functions.

Thomas et al. [104] claim that Φ' represents the phonon SED. As seen in Equation (A.28), the phonon mode eigenvectors are necessary to properly map between the atomic velocities and the normal mode coordinates. This need for the eigenvectors is the essential difference between the expressions for Φ and Φ' . The potential advantage of Φ' is that other than the wavevectors, which can be determined from the crystal structure, no phonon properties need to be known *a priori*. However, to identify the degenerate modes in Φ' , the phonon frequencies are necessary (see Section A.6.3). Since Φ' does not require the phonon mode eigenvector, it can (in principle) be used to study disordered systems or perturbed crystalline systems (e.g. dilute alloys [27], water-filled CNTs [104], and CNTs on substrates [105]). Despite its use in previous studies, Φ' has not been rigorously validated.

A.3 Interpretation of Φ'

(WORK): combine disucssion is book and also on static and dynamic-structure factor. SF can be related to the DOS(cite).

As demonstrated in Section A.8.1, Φ' is not the phonon spectral energy density, Φ , defined by Eq. (A.8). Our findings and those of others, [27, 102, 104, 106?] however, suggest that Φ' does contain accurate information about the phonon frequencies. Under the harmonic approximation, the phonons are non-interacting and have no transient response beyond a harmonic oscillation (see Appendix A.3 Eq. (A.13) and (A.17)),

$$\begin{aligned} \dot{q}(\kappa_{\nu}; t) &= \dot{q}_{SS}(\kappa_{\nu}; t) \\ &= i\omega_0(\kappa_{\nu}) \{ C_1(\kappa_{\nu}) \exp[i\omega_0(\kappa_{\nu}) t] - C_2(\kappa_{\nu}) \exp[-i\omega_0(\kappa_{\nu}) t] \}. \end{aligned} \quad (\text{A.30})$$

Inserting Eq. (A.30) into the right hand side of Eq. (A.29) gives

$$\begin{aligned} \sum_{\alpha}^3 \sum_b^n m_b \left| \sum_l^N \int_{-\infty}^{\infty} \dot{u}_{\alpha}(l; t) \exp[i\kappa \cdot \mathbf{r}_0(lal) - i\omega t] dt \right|^2 = \\ \sum_{\alpha}^3 \sum_b^n \left| \frac{m_b^{3/2}}{\sqrt{N}} \sum_l^N \sum_{\nu}^{3n} D(\kappa_b) \exp[i\kappa \cdot \mathbf{r}_0(lal)] \delta[\omega_0(\kappa_{\nu}) - \omega] \right|^2, \end{aligned} \quad (\text{A.31})$$

where $D(\kappa^b_\alpha) = i\sqrt{2\pi}\omega_0(\kappa_\nu)C_1(\kappa_\nu)e^*(\kappa^b_\alpha)$, δ is the Dirac function, and values of $\omega \leq 0$ are ignored. Thus, at zero temperature Eq. (A.27) is a superposition of Dirac functions at the phonon frequencies $\omega_0(\kappa_\nu)$.

A.4 NMD using Non-Exact Normal Modes

For a normal mode of the lattice supercell used for the MD simulations (i.e., a Gamma mode), the total energy autocorrelation is an exponential function with a decay time $\tau(\kappa_\nu)$ and the kinetic energy autocorrelation is a exponentially-damped sinusoidal oscillation with frequency $2\omega(\kappa_\nu)$.[109] When projecting MD simulations of the explicitly disordered lattice supercells onto the VC normal modes, the energy autocorrelation functions do not always follow these simple functional forms, as shown in Fig. A.1 for two modes in the LJ alloy at a concentration of 0.5. By calculating the mode kinetic energy in the frequency-domain, Φ ,[69] artifacts such as multiple peaks are observed (see main plot).

These artifacts are not surprising given two considerations: (i) the MD simulations contain explicit disorder that influences the atomic trajectories, and (ii) the VC-normal modes are not the exact normal modes of the explicitly-disordered lattice supercells. An effective lifetime can be predicted using Eq. (2.11) because the VC total mode energy autocorrelations still decay to zero in a finite time. This result is to be expected given that the atomic trajectories contain information about the lattice energy, which from general statistical physics principles will have exponential relaxation behavior in an equilibrium ensemble. [87, 110, 111]

A.5 Computational Details

A.5.1 Allowed Wavevectors

Now that we have presented the two expressions for the phonon SED, we will provide the computational details of how they can be evaluated and used to predict phonon properties. The SED is defined for the allowed wavevectors of a crystal, which can be specified from the crystal structure's Bravais lattice, its basis (i.e., unit cell), and the size of the computational domain. A D -dimensional Bravais lattice is a collection of points with positions

$$\mathbf{r}_0^{(lal)} = \sum_{\alpha}^D N_{\alpha} \mathbf{a}_{\alpha}, \quad (\text{A.32})$$

where \mathbf{a}_{α} are the lattice vectors and N_{α} is an integer [70]. The unit cell is the building block of the crystal and is placed on the points defined by the Bravais lattice. The equilibrium position of any atom in the crystal can be described by

$$\mathbf{r}_0^{(lal)} = \mathbf{r}_0^{(lal)} + \mathbf{r}_0^{(0a0)}, \quad (\text{A.33})$$

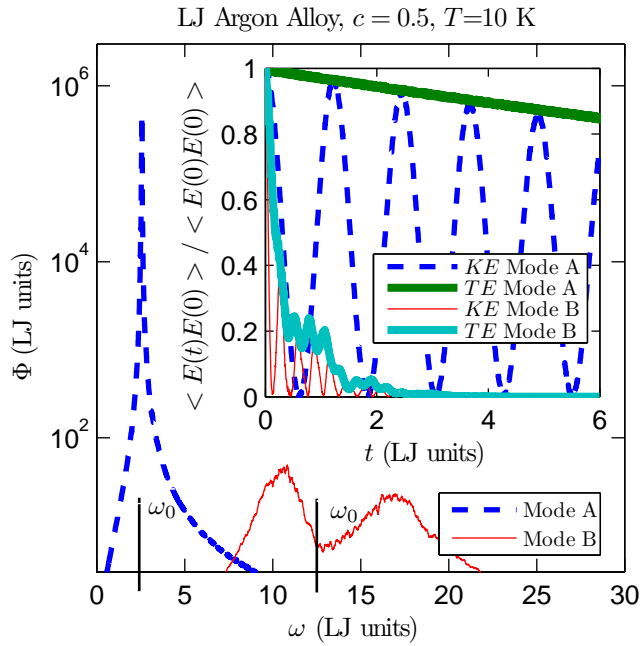


Figure A.1: The normal mode kinetic energy, Φ , of two modes (A and B) at wavevector [0.25 0 0] calculated using VC-NMD for a mass disordered LJ FCC supercell ($N_0 = 8$ and $c = 0.5$) is shown in the main figure. The VC dispersion-predicted peaks are labeled by ω_0 . The inset shows the same mode's energy [kinetic (KE) and total (TE)] autocorrelation functions. Note the additional oscillation effects in the KE and TE autocorrelation functions for Mode B which are due to the two peaks in Φ . A mode lifetime can be extracted unambiguously using the integral of the TE autocorrelation function [Eq. (2.11) in Section 2.3.3].

where $\mathbf{r}_0(0_{bbb}^{a0})$ is the equilibrium position of the b^{th} atom in the unit cell relative to $\mathbf{r}_0(0_{bb0}^{lal})$. The allowed wavevectors for any crystal structure are defined by

$$\boldsymbol{\kappa} = \sum_{\alpha} \mathbf{b}_{\alpha} \frac{n_{\alpha}}{N_{\alpha}}, \quad (\text{A.34})$$

where \mathbf{b}_{α} are the reciprocal lattice vectors and $-N_{\alpha}/2 < n_{\alpha} \leq N_{\alpha}/2$, where n_{α} are integers and N_{α} are now constant even integers. The wavevectors are taken to be in the first Brillouin zone [34].

For the LJ argon and SW silicon systems studied here, the cubic conventional cells are used with four (argon) and eight (silicon) atoms per unit cell. For the MD simulations of LJ argon and SW silicon, cubic simulation domains are used (i.e., $N_1 = N_2 = N_3 = N_0$) [3, 37, 80]. For the CNT, the Brillouin zone is one-dimensional, so that $N_1 = N_2 = 1$, and we take $N_3 = 50$ [104].

A.5.2 Symmetry Discussion

<https://github.com/ankitjainmeiitk>

<http://spglib.sourceforge.net/>

Ab initio codes such as abinit and quantum espresso also print the symmetry operations information.

$k_{ij} = k_{ji}$ and $k_{ii} = k_{jj}$ show using symmetry operations

$S = [-100; 010; 001]$

This applies to any vector or tensor property of the crystal.

[112]

lennard-jones FCC primitive conventional mapping

property(\mathbf{k}) = property($-\mathbf{k}$) for all

show how kpts are reduced to first octant using just rotations

show how kpts in first octant are reduced.

A.5.3 Phonon Lifetimes and Frequencies

Once the allowed wavevectors are specified, the atomic velocities from an MD simulation can be used to calculate Φ' using Equation (A.27). To calculate Φ [Equation (A.11)], (WORK) require the phonon mode eigenvector, which can be obtained using harmonic lattice dynamics calculations and the finite temperature lattice constant (i.e., quasi-harmonic lattice dynamics calculations) [70]. The Φ and Φ' methods can be used for any material system where there are available interatomic potentials.

The phonon frequencies and lifetimes are found by fitting the spectral curves Φ and Φ' with Lorentzian functions using a non-linear least squares method. Both of these phonon properties are independent of the Lorentzian peak magnitude. For Φ' , the different polarizations at a given wavevector are superimposed by definition of Equation (A.27). The different polarizations can be fit individually using single Lorentzian peaks or as a superposition of peaks. At high temperatures, the broadening of the peaks from different polarizations can make it difficult to uniquely locate the peaks in Φ' . Knowledge of the quasi-harmonic frequencies is necessary to identify the unique peaks in Φ' as well as degeneracies [3, 61].

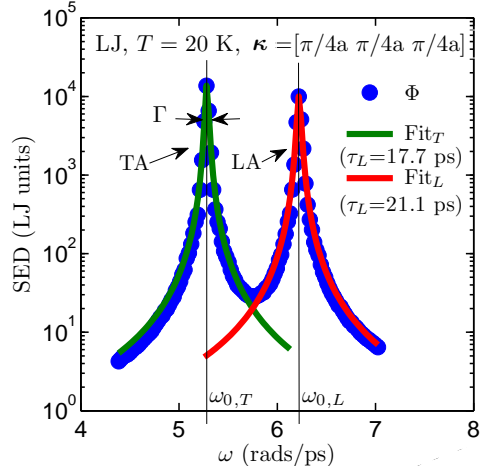


Figure A.2: The SED (using Φ) for the first three polarizations at the wavevector $[\pi/4a, \pi/4a, \pi/4a]$ for LJ argon at a temperature of 20 K. There are two degenerate transverse acoustic (TA) polarizations and one longitudinal acoustic (LA) polarization. When fitting the SED, the different polarizations can be fit individually using single Lorentzian peaks or as a superposition of polarizations. Here the two peaks are fit individually with Φ plotted as a superposition. The predicted lifetimes, which are inversely proportional to Γ are provided in the legend.

Φ has the advantage that degenerate and nearly degenerate polarizations can be isolated and fit individually. The uncertainty in the predicted phonon frequencies is on the order of the frequency resolution used to perform the fast Fourier transforms required to evaluate Φ and Φ' , which is $10^2 - 10^4$ less than the phonon frequencies studied in this work (see Sections A.8.1, A.8.2, and A.8.3). At the temperatures studied in this work, we find that fitting single or simultaneous peaks in either Φ or Φ' results in less than five percent difference in the predicted lifetimes. The uncertainty from fitting the Lorentzian functions is between five and ten percent of the predicted lifetimes, with the error increasing with increasing temperature.¹

To illustrate the procedure, Φ was calculated for LJ argon (Section A.8.1) with $N_0 = 8$ and $T = 20$ K, where T is temperature. Φ for the three modes of lowest frequency and wavevector $[\pi/4a, \pi/4a, \pi/4a]$ is shown in Fig. A.2. The lower-frequency peak corresponds to the two degenerate transverse acoustic modes, while the higher frequency peak corresponds to the longitudinal acoustic mode [70].

¹The range of data must be selected when fitting the Lorentzian functions to Φ or Φ' . This range should be large enough for the Lorentzian functions to decrease significantly from their value at half-width at half-maximum, where the linewidth is specified, but not too large as to pick up noise. The error in predicting the lifetime is obtained by varying the range of data used to fit the Lorentzian function.

A.5.4 Thermal Conductivity

Once the frequencies and lifetimes of all phonon modes in the first Brillouin zone are obtained, the bulk thermal conductivity in direction \mathbf{n} , $k_{\mathbf{n}}$, can be calculated from [19]

$$k_{\mathbf{n}} = \sum_{\boldsymbol{\kappa}} \sum_{\nu} c_{ph}(\boldsymbol{\kappa}) v_{g,\mathbf{n}}^2(\boldsymbol{\kappa}) \tau(\boldsymbol{\kappa}). \quad (\text{A.35})$$

Here, c_{ph} is the phonon volumetric specific heat and $v_{g,\mathbf{n}}$ is the component of the group velocity vector in direction \mathbf{n} . Since the systems we consider are classical and obey Maxwell-Boltzmann statistics [36], the specific heat is k_B per mode in the harmonic limit, where k_B is the Boltzmann constant. As temperature increases, anharmonicity causes the mode specific heats to deviate from k_B [37]. The effect is small for the systems and temperatures studied here. For LJ argon, the mode-averaged specific heat has been predicted to be $0.95k_B$ per mode at a temperature of 40 K and approaches k_B with decreasing temperature [37]. For SW silicon at a temperature of 300 K, the predicted mode-averaged specific heat is $1.01k_B$ per mode [38]. For the CNT at $T = 300$ K, we predict the mode-averaged specific heat to be $1.03k_B$ per mode. Because we do not have mode-dependent specific heats, we take the specific heat to be k_B per mode for the three systems studied (argon, silicon, and CNT). The group velocity vector is the gradient of the dispersion curve (i.e., $\partial\omega/\partial\boldsymbol{\kappa}$) and can be calculated from the frequencies and wavevectors using finite differences. In this work, the group velocities are calculated using the frequencies from quasi-harmonic lattice dynamics calculations because a smaller finite difference in wavevector can be used than what is available from the MD simulations (see Section A.6.1).²

A.5.5 Finite Simulation-Size Scaling for Thermal Conductivity

(WORK): add discussion from vc and mfp papers.

For the LJ argon system studied in Section A.8.1, a finite simulation-size scaling procedure [3, 4] is used to compare the thermal conductivity predictions from Φ and Φ' to those from the Green-Kubo method. The scaling procedure is demonstrated in Fig. A.3. The thermal conductivity is predicted from Φ or Φ' and MD simulations with $N_0 = 4, 6, 8$, and 10. The bulk conductivity, k_{∞} , is then estimated by fitting the data to

$$1/k = 1/k_{\infty} + A/N_0, \quad (\text{A.36})$$

where A is a constant. This procedure is necessary because the first Brillouin zone is only sampled at a finite number of points for a finite simulation size, with no contribution from the volume at its center. To predict a bulk thermal conductivity, it is important to sample points near the Brillouin zone center, where the modes can have large lifetimes and group velocities.[3, 80] As with the extrapolated bulk thermal conductivities at temperatures of 5 and 20 K (see Table A.1), the predicted thermal conductivities at each system size ($N_0 = 4, 6, 8$, and 10) are systematically smaller and outside the prediction uncertainties for Φ' compared to Φ .

²The anharmonic frequency shift affects the group velocity. McGaughey and Kaviany find that anharmonic and quasi-harmonic predictions of the group velocity differ for LJ Argon by less than one percent at a temperature of 50 K and that the difference decreases with decreasing temperature [37]. The anharmonic frequency shifts are on average a few percent for LJ argon at a temperature of 40 K and are less for the other temperatures and systems studied here.

Figure A.3: Thermal conductivity predictions for LJ argon calculated using phonon lifetimes predicted by Φ and Φ' . (a) The finite simulation-size scaling extrapolation [3, 4] is used to compare the results to bulk predictions made using the Green-Kubo method. (b) The bulk results for Φ and Green-Kubo are in good agreement temperatures of 20 and 40 K with those of other atomistic simulation methods,[3] while those from Φ' differ (see Table A.1).

A.5.6 Computational Cost

The computational cost of evaluating Equation (A.27) is less than that for Equation (A.11) by a factor of $3b$, where b is the number of atoms in the unit cell. For bulk crystals, the number of atoms in the unit cell is typically small ($b < 10$). For the (8,8) CNT system, $b = 32$ and evaluating Φ' is two orders of magnitude less expensive than evaluating Φ .

To calculate the phonon lifetimes, the MD simulation time should be an order of magnitude longer than the longest phonon lifetime [113]. If only the phonon frequencies are required, however, the location of the peaks in Φ and Φ' develop in a time on the order of the inverse of the phonon frequency, $1/\omega_0(\mathbf{k})$. For the systems studied here, this time can be two to five orders of magnitude less than the time needed to develop the lifetimes.

Fitting Φ' becomes challenging at higher temperatures, when the phonon linewidths broaden and become comparable to the spacing between mode frequencies. The cost of fitting Φ' can be reduced by fitting the peaks from all allowed wavevectors in the system simultaneously, but the error associated with this procedure is unknown [27]. We find that a semi-automated procedure, whereby the fits are visualized, is necessary to ensure that all peaks are fit correctly. While the computational cost of fitting Φ' is much smaller than the computational cost of calculating Φ' , the semi-automated fitting procedure can be of similar time cost to the user. The cost of fitting Φ is much smaller because the different polarization peaks can be isolated and the fitting can be fully automated.

A.6 Case Studies

A.6.1 Lennard-Jones Argon

We now use MD simulation to compare the SED, phonon properties, and thermal conductivity calculated for LJ argon using Φ and Φ' . The MD simulations are performed using LAMMPS [?]. A truncated and shifted potential cutoff scheme is used with a cutoff radius of 8.5 Å. The quasi-harmonic phonon frequencies, eigenvectors, and group velocities are generated using GULP [?]. We consider temperatures of 5, 20, and 40 K at zero-pressure with lattice constants of 5.278, 5.315, and 5.371 Å. For LJ argon, Turney et al. found that lattice dynamics-based predictions of thermal conductivity (e.g., by anharmonic lattice dynamics or Φ) start to diverge from MD-based predictions (e.g., from the direct or Green-Kubo methods) above half the melting temperature ($T_{\text{melt}} \approx 80$ K) [3]. Here, we limit the temperature to below half the melting temperature for the three systems studied (argon, silicon, and CNT).

The MD system consists of $N_1 \times N_2 \times N_3 = 8^3 = 512$ conventional cubic unit cells for a total of 2048 atoms ($b = 4$ atoms). Using a 4.285 fs time step, the system is equilibrated for 2^{20} time steps before collecting data every 2^5 time steps for an additional 2^{20} time steps in the *NVE* ensemble (constant number of atoms, system volume, and total system energy) [36]. The sampling rate must be high enough to capture the highest phonon frequency in the system. The sampling rate and total run time are chosen in powers of two as a convenience in performing the fast Fourier transforms required to efficiently evaluate Φ and Φ' . The same MD simulation data are used to calculate Φ and Φ' . Five simulations with different initial conditions are performed and the Φ and Φ' values are averaged before the peak fitting. Φ and Φ' are further averaged over degenerate wavevectors in the Brillouin zone, reducing the wavevectors to the first octant [53].

The SED (Φ and Φ') for the wavevector $[\pi/2a, 0, 0]$ is presented in Fig. A.4 for all three temperatures (the edge of the Brillouin zone is at $[\pi/a, 0, 0]$). For Φ , the spectral curve is plotted as a superposition over the twelve phonon polarizations, with degeneracy reducing the number of peaks to seven. Overall, Φ' does not equal the total phonon spectral energy density Φ , but the major features are similar. At all temperatures there are linewidth variations between the two spectral curves. The peak magnitudes become comparable for Φ and Φ' as the temperature increases. The phonon frequencies and lifetimes extracted for all allowed wavevectors in the first Brillouin zone using Φ and Φ' at each of the three temperatures are compared on a mode-by-mode basis in Figs. A.5(a), A.5(b), and A.5(c). There, ω_0 , ω'_0 , τ , and τ' refer to the mode properties predicted using Φ and Φ' . The phonon frequencies agree well at all three temperatures, with increasing scatter at high temperatures and high frequencies. This scatter is due to the high-frequency peak broadening seen in Fig. A.4 at $T = 40$ K, which can force peaks close in frequency for Φ' to be fit as a single Lorentzian function. The frequencies predicted by Φ and Φ' include the effects of anharmonicity, which increase the frequencies compared to the quasi-harmonic predictions [3, 61]. The agreement between the frequencies predicted from Φ and Φ' is explained in (REF) (WORK).

The lifetimes show large scatter between Φ and Φ' on a mode-by-mode basis, with increasing scatter at high temperature that shows no systematic difference. The scatter at high frequencies is in part due to the peak broadening seen in Fig. A.4, which can force peaks close in frequency for Φ' to be fit as a single Lorentzian function with a single lifetime. The broadening does not

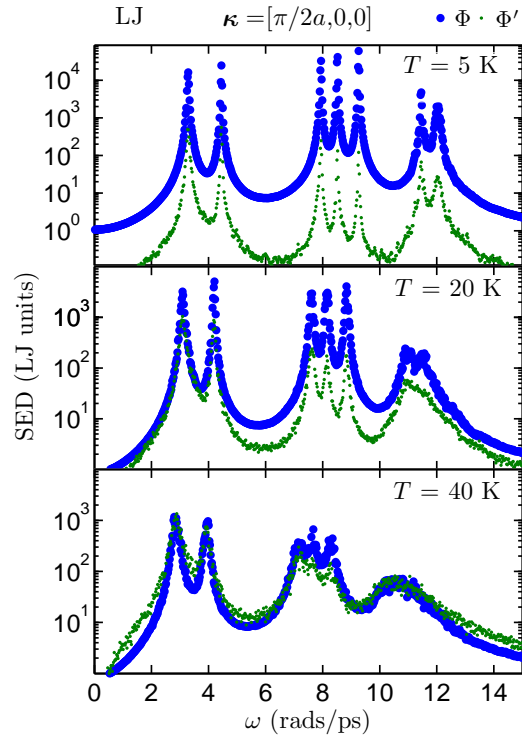


Figure A.4: The phonon spectral energy density (Φ) is plotted as larger blue circles. The proposed alternative expression for the phonon spectral energy density (Φ') is plotted as smaller green points. The wavevector is $(\pi/2a, 0, 0)$. Note that peak broadening at higher temperatures and frequencies above 10 rads/ps can force peaks close in frequency for Φ' to be fit as a single Lorentzian function. Φ does not suffer from this issue since the broadened peaks can be fit individually.

Table A.1: Thermal conductivity values in W/m-K predicted using the Φ , Φ' , and Green-Kubo methods. The predictions for Φ and Green-Kubo for the LJ system are in good agreement with those from other atomistic simulation methods [3] while those from Φ' differ and show no consistent behavior. The uncertainties in the predicted thermal conductivities for Φ and Φ' come predominantly from the finite simulation-size scaling procedure (see Ref. [3, 4]), where the phonon properties and thermal conductivity are predicted for increasing system sizes ($N_1 = N_2 = N_3$) to extrapolate a bulk thermal conductivity. For SW silicon and the CNT, the extrapolation procedure is not performed.

T (K)	Green-Kubo	Φ	Φ'
LJ (bulk)			
5	8.0 ± 0.30	7.9 ± 0.42	5.8 ± 0.31
20	1.3 ± 0.15	1.2 ± 0.07	1.0 ± 0.10
40	0.45 ± 0.07	0.47 ± 0.03	0.49 ± 0.05
SW ($N_1 = N_2 = N_3 = 6$)			
300		322 ± 16	396 ± 38
CNT ($N_1 = N_2 = 1, N_3 = 50$)			
300		428 ± 21	398 ± 40

affect fitting at low frequencies, where the linewidths are much smaller than the peak spacings. There, any scatter comes solely from the difference between Φ and Φ' .

The phonon properties are then used to predict thermal conductivity using Equation (A.35). The results are presented in Table A.1. The bulk thermal conductivities provided in Table A.1 are predicted using the finite simulation-size scaling procedure discussed in [3]. The bulk thermal conductivities predicted from Φ' are smaller and outside the uncertainty for those predicted from Φ for temperatures of 5 and 20 K. While the bulk thermal conductivities at a temperature of 40 K agree within their uncertainties, the predicted mode-by-mode lifetimes show large scatter [Fig. A.5(c)] and the agreement should be regarded as coincidental.

The disagreement between Φ and Φ' in thermal conductivity comes directly from the differences in the phonon lifetimes. All other properties (frequencies, group velocities, specific heats) are nearly or exactly the same for the two calculations. The bulk thermal conductivities predicted from Φ and Φ' are also compared to predictions from the Green-Kubo method[36] in Table A.1. For $N_1 = N_2 = N_3 = 8$, the thermal conductivity predicted by the Green-Kubo method is converged with respect to the simulation size [37]. The same MD data used to calculate Φ and Φ' is used for the Green-Kubo predictions. For all three temperatures, there is good agreement between the thermal conductivity predictions using Φ and Green-Kubo. For temperatures of 20 and 40 K, there is good agreement between the predictions from Φ , Green-Kubo, and previous reports using non-equilibrium MD, anharmonic lattice dynamics, and time-domain Φ [3].

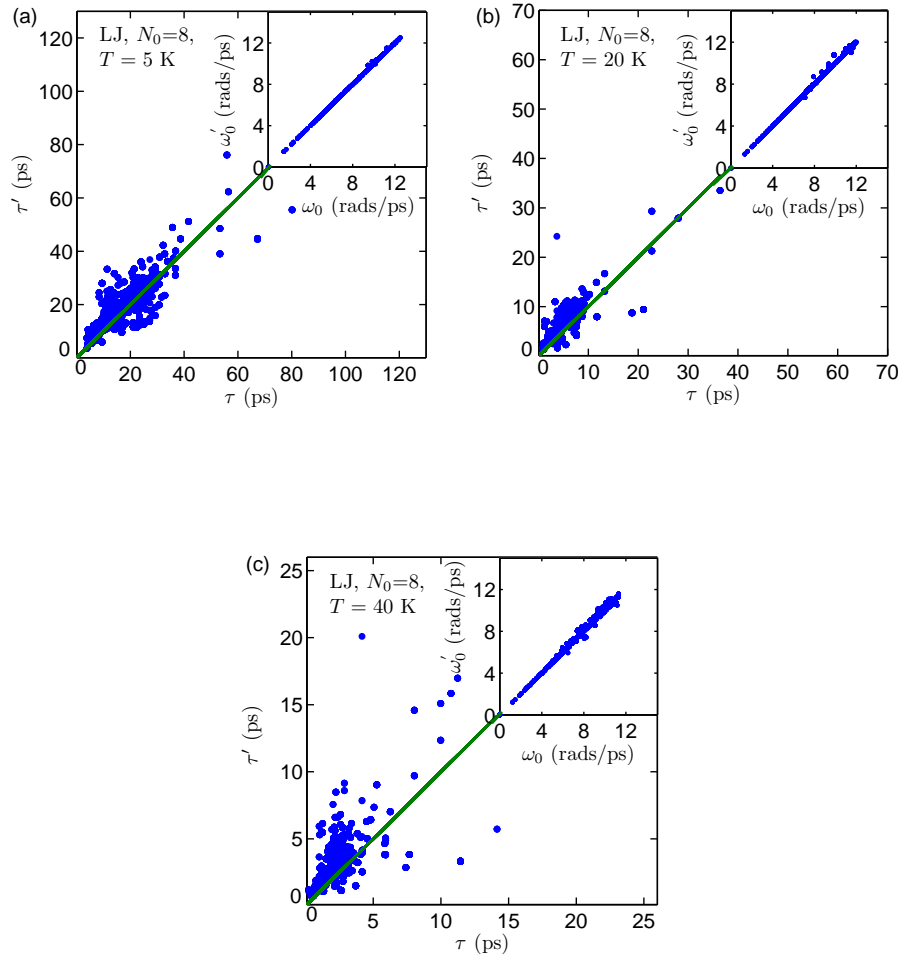


Figure A.5: Comparison of the phonon frequencies and lifetimes predicted using Φ (ω and τ) and Φ' (ω' and τ') for LJ argon at temperatures of (a) 5 K, (b) 20 K, and (c) 40 K. The phonon frequencies agree well at all three temperatures, while the phonon lifetimes show large scatter.

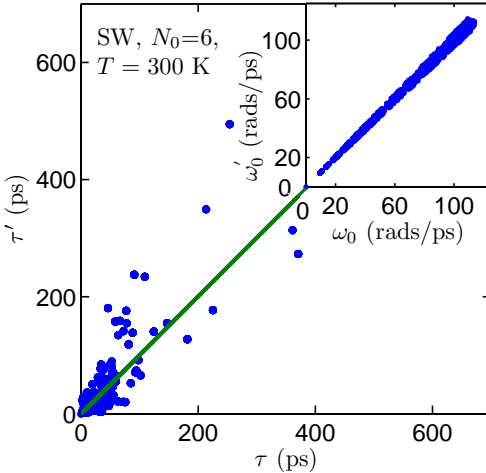


Figure A.6: Comparison of the phonon frequencies and lifetimes predicted using $\Phi(\omega \text{ and } \tau)$ and $\Phi'(\omega' \text{ and } \tau')$ for SW silicon. The phonon frequencies agree well, while the phonon lifetimes show large scatter.

A.6.2 Stillinger-Weber Silicon

We next compare the phonon properties and thermal conductivity predicted from Φ and Φ' for SW silicon [35] at a temperature of 300 K and zero pressure with a lattice constant of 5.437 Å. The SW system is stiffer (larger phonon group velocities, frequencies, and lifetimes) than LJ argon and is an additional test to determine if there is a systematic error in the predictions from Φ' . The MD simulations are performed using LAMMPS [54]. The MD system consists of $N_1 \times N_2 \times N_3 = 6^3 = 216$ conventional unit cells for a total of 1728 atoms ($b = 8$ atoms). The phonon frequencies, eigenvectors, and group velocities are generated using GULP [57].

Using a 0.5 fs timestep, the system is equilibrated for 2^{20} time steps before collecting data every 2^5 time step for 2^{22} time steps in the NVE ensemble [36]. As with the LJ system, the sampling rate is determined by the highest phonon frequency in the system. Five simulations with different initial conditions are performed and the Φ and Φ' values are averaged before the peak fitting. Φ and Φ' are further averaged over degenerate wavevectors in the Brillouin zone, reducing the wavevectors to the first octant [53].

The extracted phonon frequencies and lifetimes are plotted in Fig. A.6. As with the LJ system, the phonon frequencies are predicted accurately by Φ' but the lifetimes show large scatter on a mode-by-mode basis. For the system size studied, Φ' predicts a larger thermal conductivity than Φ outside the prediction uncertainties, in contrast to the LJ system (see Table A.1). The disagreement in thermal conductivity comes directly from the phonon lifetimes.

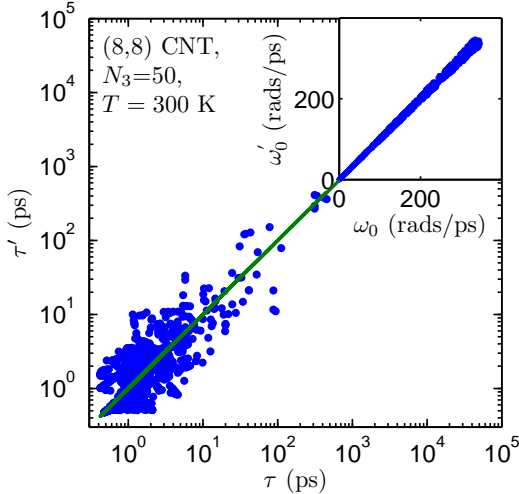


Figure A.7: Comparison of the phonon frequencies and lifetimes predicted using $\Phi(\omega, \tau)$ and $\Phi'(\omega', \tau')$ for a (8,8) CNT modeled using the REBO potential. The phonon frequencies agree well, while the phonon lifetimes show large scatter.

A.6.3 Carbon Nanotube

Finally, we compare the phonon properties and thermal conductivities predicted by Φ and Φ' for an (8,8) CNT (diameter of 1.10-nm and length of 12.3 nm) at a temperature of 300 K and zero pressure [104]. The interactions in the CNT system are modeled using the REBO potential without the four-body interaction term [?]. The MD simulations are performed using an in-house code. The MD system consists of 1600 atoms (32 atoms/unit cell). The phonon frequencies, eigenvectors, and group velocities are generated using an in-house code. The purpose of simulating this system is to check the results of Thomas et al. [104] (who used Φ' and non-equilibrium MD), and to compare the predictions of Φ' and Φ .

Using a 1.0 fs timestep, the system is equilibrated for 2^{20} time steps before collecting data every 2^3 time step for 2^{22} time steps in the NVE ensemble [36]. As with the LJ and SW systems, the sampling rate is determined by the highest phonon frequency in the system. Five simulations with different initial conditions are performed and the Φ and Φ' values are averaged before the peak fitting. Since the Brillouin zone of the CNT is one-dimensional, Φ and Φ' are further averaged over directionally-degenerate wavevectors.

The phonon frequencies and lifetimes for the allowed wavevectors in the one-dimensional Brillouin zone are shown in Fig. A.7. Like the LJ and SW silicon systems, the phonon frequencies can be predicted accurately by Φ' , but the lifetimes show large scatter. The estimated thermal conductivity of the CNT predicted using Φ' is in agreement with the results of Thomas et al. [104]. The thermal conductivity predicted by Φ' is less than that predicted by Φ , but not outside their uncertainties.

A.7 Summary

We presented the correct phonon SED, Φ , and its relation to the phonon frequencies and lifetimes. We then presented an alternative formulation to the phonon spectral energy density, Φ' , which does not require the phonon mode eigenvectors. Because Φ' does not contain the eigenvectors, this alternative formulation does not represent the phonon spectral energy density, but does contain information about the phonon dispersion as the temperature approaches 0 K (see (REF) (WORK)).

We then calculated the phonon SED for LJ argon, SW silicon, and a CNT modeled with the REBO potential using Φ and Φ' . The phonon frequencies and lifetimes predicted from Φ and Φ' are shown in Figs. A.5, A.6 and A.7. The frequencies are in good agreement between the two SED methods, while the lifetimes show large scatter.

The phonon SED Φ is well-defined theoretically, while Φ' does not properly map to the phonon energies since it is missing the phonon mode eigenvector. We deduce that this is the reason Φ' does not accurately predict the phonon lifetimes. It is surprising how close the predicted thermal conductivities can be using Φ and Φ' (LJ at $T = 40$ K and the CNT results). The thermal conductivities predicted by Φ and Φ' , however, show no consistency for the three systems studied.

The most important predictions are the mode-by-mode phonon properties. Of particular importance are the lifetimes, which are the key input for Boltzmann transport equation-based models [99]. Thus, we do not recommend Φ' for predicting phonon lifetimes or thermal conductivity. Any agreement in thermal conductivity predictions between atomistic studies[104] and experiment [106?] should be regarded as coincidental, and the phonon lifetime reductions predicted for systems with additional scattering methods [27, 104] should only be interpreted qualitatively. The use of Φ' in future work is discouraged and we reccomend the use of Φ .

This work is supported by AFOSR award FA95501010098. We thank John A. Thomas (Johns Hopkins University Applied Physics Laboratory) for helpful discussions.

July 24, 2013
DRAFT

Appendix B

Research using High Performance Computing

B.1 Setting Up Computing Environment

B.1.1 Hardware and Operating System Choice

The choice of hardware determines the operating system. The three main choices for operating system are Windows, Apple OS, and Linux. Each operating system has limitations depending on the hardware it operates on. For example, Apple OS is primarily used on Apple hardware.

Linux: world's most widely used software Linux runs on cell phones to the world's largest supercomputers. Recommend the most widely used linux version ubuntu. well-documented, large-community discussion Apple OS is an adequate substitute as it is unix-like.

There are many options for installing Ubuntu and the instructions can be found on <http://www.ubuntu.com/>. Ubuntu is certified on many top PC's from many computer companies and a company, system 76, builds computers with Ubuntu pre-installed. I used the Pangolin Performance for over a year of my PhD. However, I recommend using the lightest, most-portable, and longest-battery life notebook available such as the Samsung Series 9 or Macbook Air. You will typically be using this notebook to access large computing clusters remotely, so there is a benefit of having portability and long battery life over large computational power.

B.1.2 System Terminal and Commands

These instructions work best for Ubuntu operating system, and will work well for other versions of Linux. Systems commands are executed by the system terminal.

Useful Linux Commands:

sed, grep, ls, cd, pwd, export, setenv, scp -r, ssh, sudo, nohup, vi, cat, which, echo
google: linux sed

B.1.3 Environment Variables

environment variable such as \$PATH. Here is how we determine what PATH is set to:

Set PATH for lammps (see Section).

Permanent changes to environment variables can be made in the user's .bashrc file, which is typically located in the /home/user/ directory. The .bashrc file is a hidden file noted by its name starting with ". ". Other

Here is an example .bashrc which demonstrates how to add permanent paths and how to define new functions within the operating system. For example, to copy the output of the pwd command to the system's clipboard, use cpyc then "ctrl-v" elsewhere.

This file modifies environment variables such as PATH when a bash terminal session is launched. Changes to environment variables are made when a new terminal session is started. The location of this file is typically: /home/user/.bashrc. The

.bashrc from Kevin Parrish.

B.1.4 Shell Scripts and System Commands in Python

Shell scripts are relatively low-level scripts which execute system commands (Section) and manipulate environment variables (Section) of the Linux operating system.

Here is a simple tutorial on writing shell scripts <http://linuxcommand.org/wss0010.php>

Running Linux system commands in Python can be an effective way of generating and manipulating many files with one script. Python is a more robust language than lower-level shell scripting. Here is an example:

lmp.in.iseed

B.1.5 Remote Resources Commands

At some point during research you will need to execute code on remote resources which are typically large (100 cpu) computing clusters. You will be provided with a terminal session similar to the session provided by Ubuntu with most of the same system commands.

While I recommend Filezilla for handling the transfer of data and files, the functionality of Filezilla is contained in several shell commands:

ssh user@gilgamesh.cheme.cmu.edu

or equivalently by the machine's ip address:

ssh user@xxx.xxx.xxx.xxx

Files can be transferred using the following command:

scp -r user@gilgamesh.cheme.cmu.edu:/home/user/directory/ ./

which will place the "directory" and its contents into the pwd (./) of the local terminal session.

There are many variants of the operating systems used for remote computing clusters, but the differences are usually superficial. During my work I used the gilgamesh computing cluster maintained by John Kitchin. Gilgamesh's documentation is a good resource for learning how to run calculations on a computing cluster.

B.1.6 Installing Programs

Ubuntu and similar linux OS have automatic software installation and management using the apt-get system command:

```
jason@jason-900X3C / (master) $ sudo apt-get install gfortran [sudo] password for jason:
Reading package lists... Done Building dependency tree Reading state information... Done
gfortran is already the newest version. The following package was automatically installed and is
no longer required: kde-l10n-engb Use 'apt-get autoremove' to remove it. 0 upgraded, 0 newly
installed, 0 to remove and 129 not upgraded.
```

To check that the package has been installed, use:

```
jason@jason-900X3C-900X3D-900X3E-900X4C-900X4D / (master) $ which gfortran /usr/bin/gfortran
```

This shows that gfortran program is installed in the /usr/bin/ folder, a common location where automatically installed programs are located. Because the folder /usr/bin is in the PATH environment variable:

the program gfortran is always available no matter where you are in the system terminal.

To get more information about the gfortran, use:

```
jason@jason-900X3C / (master) $ ls -l /usr/bin/gfortran lrwxrwxrwx 1 root root 12 Apr 22
03:44 /usr/bin/gfortran -> gfortran-4.7
```

where we see that /usr/bin/gfortran "points" to gfortran-4.7. This is called a symbolic link, which can be created using:

```
jason@jason-900X3C /disorder/pcbm/topotools-tutorial-part2 (master) $ ls -l /usr/bin/gfortran lrwxrwxrwx 1 root root 12 Apr 22 03:44 /usr/bin/gfortran -> gfortran-4.7
```

B.1.7 Available Programs

Available programs represent opportunities to perform research quickly and easily. I suggest you read their documentation carefully and try the tutorials which are typically computationally inexpensive.

Install lammps:

Set PATH for lammps

gnu compilers vs intel: gnu freely available tar -zxvf lammps.tar, make serial, sudo apt-get install openmpi, make openmpi

open-source:

LAMMPS, including the particularly useful mailing list (use ctrl-f to search on any topic) and python interface which is used with the package ntpy. GULP, ABINIT, Quantum Espresso, VESTA, phonopy, VMD (with topotools) ntpy, VASP DL_{POLY}, siesta, GAMESS, CP2K, BOLTZTRAP, PHON,

I recommend trying this install.sh created by Kevin Parrish which installs many programs and packages, including lammps for parallel computing with openmpi.

B.2 Preparing Journal Articles and Thesis

recommendation: student advisor should try and exchange editing a written research document at least every week. The exchange of such a document

Such a research document could be the running collection of journal articles which turn into the thesis. Maintenance of this document can be achieved with Dropbox or Github. Github offers to advantage of smart version control and a built-in wiki.

B.2.1 Journal Articles

The job of the student is to prepare, submit, and publish peer-reviewed journal articles. There are many journals suitable for nanoscale transport topics. All of them accept Latex prepared manuscripts. I recommend the Latex editor Kile, while the simple gedit works well and comes pre-installed with Ubuntu. Here is a simple latex example and how to generate a portable document format (PDF) from the latex document.

To maintain the reference library I recommend zotero. Here is an example reference.bib file which is exported automatically by zotero. The references are generated from the latex document using bibtex which compiles the contents of the reference.bib.

Here is an example of the latex files used to create an article published from this work:

Predicting alloy properties.

This file uses revtex, which is an article class used by Physical Review, Journal of Applied Physics, and others.

B.2.2 Thesis

These can be used as templates

Here is a Carnegie Mellon thesis template:

<https://github.com/robsimmons/cmu-thesis>

J. Larkin thesis files.

Article on structuring large documents.

B.3 Technical Advice

In addition to your advisor and close mentors, I reccomend communicating with experts in the field as much as possible without being an annoying. How often to communicate depends on the situation. It is best to let the expert dictate the pace of the conversation.

B.3.1 Expert Advice

Here is a list of experts I used as resources for this work. They will typically answer emails within 24-48 hours:

Alan McGaughey, Jon Malen, Julian Gale (GULP author), Keivan Esfarjani, normand.mousseau@umontreal
guido.raos@polimi.it, Joseph Feldman, Junchiro Shiomi, Davide Donadio, Craig Maloney, Jivtesh Garg,
John Duda, Wissam Al-Saidi, Dan Sellan, Ankit Jain, Wee-Liat Ong, John Kitchin, Steve Plimpton via the LAMMPS mailing list Axel Kolhmeyer via the LAMMPS mailing list and email

Atz Togo, creator of phonopy

me

B.3.2 Online Resources

wikipedia
octave
https://en.wikipedia.org/wiki/Lennard-Jones_potential
http://www.sklogwiki.org/SklogWiki/index.php/Lennard-Jones_model
we can do better, needs to be organization.
<http://nanohub.org/>
does not provide good HPC resources.

B.4 Coding Languages: Compiled versus Interpreted

There are many languages used for the open-source and licensed packages(REF) that can be used to study nanoscale transport. These packages use compiled and interpreted languages and often a mixture of the two.

The most commonly used compiled languages are C/C++ (linux, LAMMPS) and Fortran (GULP, quantum espresso, VASP).

A good discussion on the strengths of C++ versus Fortran.

excellent c++ tutorial

excellent fortran tutorial

The two interpreted languages you are likely to use are matlab and python.

The key to maximizing the potential of interpreted languages is by using the built-in “vector” functions and operations provided by the matlab and python programming libraries.

matlab has an excellent built-in guide, google search will typically yield useful results. A good open-source substitute for matlab is octave which is capable of running most matlab scripts.

B.4.1 Compiled Language Case-study: Lennard-Jones Argon Molecular Dynamics

The first case study is a single C code to perform Molecular Dynamics on LJ argon. The code is a serial code with

/home/jason/classes/cmu/molecular_simulation/HW5

Listing B.1: Some Code

```
jason@jason-900X3C ~ / classes / cmu / molecular_simulation / HW5 ( master ) c++ ArgonM
```

Listing B.2: Some Code

```
jason@jason-900X3C ~ / classes / cmu / molecular_simulation / HW5 ( master ) ./ArgonM
```

The output is. A useful shell operation is ”piping”, which is demonstrated below:

Listing B.3: Some Code

```
jason@jason-900X3C ~ / classes / cmu / molecular_simulation / HW5 ( master ) $ ./ArgonM
```

Another useful shell command is ”vi”, a shell-based text editor:

Listing B.4: Some Code

```
jason@jason-900X3C ~/classes/cmu/molecular_simulation/HW5 (master) $ vi pro
5.61358 2.01864 5.26596
3.4073 1.72339 1.32187
5.28007 0.107792 4.95407
1.45285 5.09976 0.961697
4.5679 4.82261 5.78293
5.29423 0.880753 0.709709
3.63248 5.45978 2.70637
...
```

B.4.2 Compiled versus Interpreted Case-study(a): Lennard-Jones Dispersion

With interpreted languages traditional programming practice of using loops (for/do/while, etc) will slow the code down.

Matlab version using mixture of loops and vectorized functions.

Fortran version (GULP)

B.4.3 Compiled versus Interpreted Case-study(b): Allen-Feldman Diffusivity Calculation

Two systems, my local laptop:

<http://www.samsung.com/us/computer/series-9-notebooks>

Listing B.5: Some Code

```
jason@jason-900X3C ~/disorder (master) $ $$ cat /proc/cpuinfo
processor : 0
vendor_id : GenuineIntel
cpu family : 6
model : 58
model name : Intel(R) Core(TM) i5-3317U CPU @ 1.70GHz
stepping : 9
microcode : 0x17
cpu MHz : 782.000
cache size : 3072 KB
physical id : 0
siblings : 4
core id : 0
cpu cores : 2
apicid : 0
initial apicid : 0
```

and gilgamesh
<http://gilgamesh.cheme.cmu.edu/doc/gilgamesh.html>

Listing B.6: Some Code

```
jason@gilgamesh > cat /proc/cpuinfo
processor       : 0
vendor_id      : AuthenticAMD
cpu family     : 16
model          : 9
model name     : AMD Opteron(tm) Processor 6128 HE
stepping        : 1
cpu MHz         : 2000.003
cache size      : 512 KB
physical id     : 1
siblings         : 8
core id          : 0
cpu cores        : 8
apicid           : 16
```

B.4.4 Scaling Calculations

The majority of the methods used in this work scale poorly with the number of atoms, N_a^α with $\alpha > 1$.

Let's take the scaling cost N_a^3 , which is the scaling for eigenvalue solution used in Sections . The cost of performing this calculation for a large system size $N_{a,large}$ and every successive system which is half the size of the former is given by the geometric series with common ratio $r = 1/8$

$$cost_{total} = N_{a,large} \frac{1}{1 - r} = 1.143 N_{a,large} \quad (\text{B.1})$$

It costs a minimal amount ($\tilde{14}\%$) to study every system smaller than the largest system considered. Even a linear scaling N_a has $cost_{total} = 2N_{a,large}$. Because of this I recommend picking the system of maximum size and then start calcualtions with the smallest system of interest. Publication drafts can be developed mush faster by performing computationally cheap calculations first, documenting the results, and then iterating to more computationally expensive calculations. This scheme for performing calculations can follow these time-scales for calculation costs: one second, minute, hour, day, and week. I have performed countless calculations costing around one second and very few which cost more than one week. Publication quality results will typically cost between one hour and one week.

July 24, 2013
DRAFT

Bibliography

- [12] Eric S. Toberer, Alex Zevalkink, and G. Jeffrey Snyder. Phonon engineering through crystal chemistry. *J. Mater. Chem.*, 21(40), 2011. 2.1
- [13] M. Zebarjadi, K. Esfarjani, M. S. Dresselhaus, Z. F. Ren, and G. Chen. Perspectives on thermoelectrics: from fundamentals to device applications. *Energy Environ. Sci.*, 5(1):51475162, 2012. 2.1
- [14] Scott N. Schiffres, Kyu Hun Kim, Lin Hu, Alan J. H. McGaughey, Mohammad F. Islam, and Jonathan A. Malen. Gas diffusion, energy transport, and thermal accommodation in single-walled carbon nanotube aerogels. *Advanced Functional Materials*, 22(24):52515258, December 2012. 2.1
- [15] Shin-ichiro Tamura. Isotope scattering of dispersive phonons in ge. *Phys. Rev. B*, 27(2):858866, January 1983. 2.1, 2.2.2, 2.3.3, 2.3.3, 2.3.3, 2.5
- [16] L. Lindsay, D. A. Broido, and T. L. Reinecke. Thermal conductivity and large isotope effect in GaN from first principles. *Phys. Rev. Lett.*, 109(9):095901, August 2012. 2.1, 2.2.1, 2.2.2, 2.5, 2.6
- [17] B. Abeles, D. S. Beers, G. D. Cody, and J. P. Dismukes. Thermal conductivity of ge-si alloys at high temperatures. *Phys. Rev.*, 125(1):4446, January 1962. 2.1, 2.6
- [18] B. Abeles. Lattice thermal conductivity of disordered semiconductor alloys at high temperatures. *Phys. Rev.*, 131(5):19061911, September 1963. 2.1, 2.2.2, 2.6
- [19] J. M. Ziman. *Electrons and Phonons*. Oxford, New York, 2001. 2.1, 2.2.1, 2.3.3, A.6.4
- [20] Joseph L. Feldman, Mark D. Kluge, Philip B. Allen, and Frederick Wooten. Thermal conductivity and localization in glasses: Numerical study of a model of amorphous silicon. *Physical Review B*, 48(17):1258912602, November 1993. 2.1, 2.2.1, 2.3.4, 2.3.4, 2.3.5
- [21] P. B. Allen, J. L. Feldman, J. Fabian, and F. Wooten. Diffusons, locons, and propagons: character of atomic vibrations in amorphous si. *Philosophical Magazine B*, 79:17151731, 1999. 2.1, 2.3.2, 2.3.2, 2.6
- [22] D. A. Broido, M. Maloney, G. Birner, N. Mingo, and D. Stewart. Intrinsic lattice thermal conductivity of semiconductors from first principles. *Applied Physics Letters*, 91:231922, 2007. 2.1, 2.2.1, A.1
- [23] A. Ward and D. A. Broido. Intrinsic phonon relaxation times from first-principles studies of the thermal conductivities of si and ge. *Phys. Rev. B*, 81(8):085205, February 2010. 2.1, 2.2.1, 2.6
- [24] Jivtesh Garg, Nicola Bonini, Boris Kozinsky, and Nicola Marzari. Role of disorder and anharmonicity in the thermal conductivity of silicon-germanium alloys: A first-principles study. *Phys. Rev. Lett.*, 106(4):045901, January 2011. 2.1, 2.2.1, 2.2.2, 2.3.1, 2.3.3, 2.3.3, 2.5, 2.6
- [25] Takuma Shiga, Junichiro Shiomi, Jie Ma, Olivier Delaire, Tomasz Radzynski, Andrzej Lusakowski, Keivan Esfarjani, and Gang Chen. Microscopic mechanism of low thermal conductivity in lead telluride. *Phys. Rev. B*, 85(15):155203, April 2012. 2.1, 2.2.2, 2.6
- [26] Zhiting Tian, Jivtesh Garg, Keivan Esfarjani, Takuma Shiga, Junichiro Shiomi, and Gang Chen. Phonon conduction in PbSe, PbTe, and PbTe\$-1\$-\$x\$Se\$-x\$ from first-principles

- calculations. *Phys. Rev. B*, 85(18):184303, May 2012. 2.1, 2.2.2, 2.3.3, 2.3.3, 2.5, 2.6
- [27] Junichiro Shiomi, Keivan Esfarjani, and Gang Chen. Thermal conductivity of half-heusler compounds from first-principles calculations. *Physical Review B*, 84(10):125209, 2011. 2.1, 2.4, 2.6, A.1, A.2.1, A.3, A.3.1, A.4, A.7.1, A.9
- [28] K. Esfarjani, G. Chen, and H. T. Stokes. Heat transport in silicon from first-principles calculations. *Physical Review B*, 84:085204, 2011. 2.1, 2.2.2, 2.4, 2.5, 2.6, A.1
- [29] Wu Li, L. Lindsay, D. A. Broido, Derek A. Stewart, and Natalio Mingo. Thermal conductivity of bulk and nanowire Mg₂Si_xSn_{1-x} alloys from first principles. *Phys. Rev. B*, 86(17):174307, November 2012. 2.1, 2.2.2, 2.3.3, 2.6
- [30] Maria N. Luckyanova, Jivtesh Garg, Keivan Esfarjani, Adam Jandl, Mayank T. Bulsara, Aaron J. Schmidt, Austin J. Minnich, Shuo Chen, Mildred S. Dresselhaus, Zhifeng Ren, Eugene A. Fitzgerald, and Gang Chen. Coherent phonon heat conduction in superlattices. *Science*, 338(6109):936939, 2012. 2.1, 2.2.2, 2.6
- [31] A. Ward, D. A. Broido, Derek A. Stewart, and G. Deinzer. Ab initio theory of the lattice thermal conductivity in diamond. *Phys. Rev. B*, 80(12):125203, September 2009. 2.1, 2.2.1
- [32] Hua Bao, Bo Qiu, Yu Zhang, and Xiulin Ruan. A first-principles molecular dynamics approach for predicting optical phonon lifetimes and far-infrared reflectance of polar materials. *Journal of Quantitative Spectroscopy and Radiative Transfer*, 113(13):1683–1688, 2012. 2.1
- [33] Gabriele C. Sosso, Davide Donadio, Sebastiano Caravati, Jrg Behler, and Marco Bernasconi. Thermal transport in phase-change materials from atomistic simulations. *Phys. Rev. B*, 86(10):104301, September 2012. 2.1
- [34] N. W. Ashcroft and N. D. Mermin. *Solid State Physics*. Saunders, Fort Worth, 1976. 2.1, 2.3.1, 2.3.3, A.1, A.6.1
- [35] F. H. Stillinger and T. A. Weber. Computer simulation of local order in condensed phases of silicon. *Physical Review B*, 31:52625271, 1985. 2.1, 2.3.3, A.1, A.8.2
- [36] D. A. McQuarrie. *Statistical Mechanics*. University Science Books, Sausalito, 2000. 2.2.1, A.3, A.6.4, A.8.1, A.8.1, A.8.2, A.8.3
- [37] A. J. H. McGaughey and M. Kaviany. Quantitative validation of the boltzmann transport equation phonon thermal conductivity model under the single-mode relaxation time approximation. *Physical Review B*, 69:094303, 2004. 2.2.1, 2.3.3, 2.4, A.1, A.2.1, A.3, A.6.1, A.6.4, 2, A.8.1
- [38] J. V. Goicochea, M. Madrid, and C. H. Amon. Thermal properties for bulk silicon based on the determination of relaxation times using molecular dynamics. *Journal of Heat Transfer*, 132:012401, 2010. 2.2.1, 2.2.3, A.1, A.2.1, A.3, A.6.4
- [39] Philip B. Allen and Joseph L. Feldman. Thermal conductivity of disordered harmonic solids. *Physical Review B*, 48(17):1258112588, November 1993. 2.2.1, 2.2.1, 2.3.4, 2.3.5, 2.6
- [40] Joseph L. Feldman, Philip B. Allen, and Scott R. Bickham. Numerical study of low-

- frequency vibrations in amorphous silicon. *Phys. Rev. B*, 59(5):35513559, February 1999. 2.2.1, 2.3.2, 2.3.2, 2.3.4, 2.3.5
- [41] P. G. Klemens. The scattering of low-frequency lattice waves by static imperfections. *Proceedings of the Physical Society. Section A*, 68(1113), 1955. 2.2.2, 2.3.3, 2.3.3
- [42] P. G. Klemens. Thermal resistance due to isotopic mass variation. *Proceedings of the Physical Society. Section A*, 70(11):833, 1957. 2.2.2, 2.3.3, 2.3.3
- [43] J. Callaway. Model for lattice thermal conductivity at low temperatures. *Physical Review*, 113:1046, 1959. 2.2.2, 2.3.3, A.1
- [44] Daniel Charles Mattis. Phonon free path in an isotopic mixture. *Phys. Rev.*, 107(6):17361736, September 1957. 2.2.2, 2.3.3, 2.3.3
- [45] W. A. Kamitakahara and B. N. Brockhouse. Vibrations of a mixed crystal: Neutron scattering from $\text{Ni}_{55}\text{Pd}_{45}$. *Phys. Rev. B*, 10(4):12001212, August 1974. 2.2.2, 2.6
- [46] David G. Cahill and Fumiya Watanabe. Thermal conductivity of isotopically pure and ge-doped si epitaxial layers from \$300\text{SiGe}/\text{Si}\$. *Phys. Rev. B*, 70(23):235322, December 2004. 2.2.2, 2.6
- [47] David G. Cahill, Fumiya Watanabe, Angus Rockett, and Cronin B. Vining. Thermal conductivity of epitaxial layers of dilute SiGe alloys. *Phys. Rev. B*, 71(23):235202, June 2005. 2.2.2, 2.6
- [48] Ashton Skye and Patrick K. Schelling. Thermal resistivity of SiGe alloys by molecular-dynamics simulation. *Journal of Applied Physics*, 103(11):113524, 2008. 2.2.2
- [49] E. S. Landry and A. J. H. McGaughey. Thermal boundary resistance predictions from molecular dynamics simulations and theoretical calculations. *Physical Review B*, 80:165304, 2009. 2.2.2, A.1
- [50] Zhiting Tian, Keivan Esfarjani, and Gang Chen. Enhancing phonon transmission across a Si/Ge interface by atomic roughness: First-principles study with the green's function method. *Phys. Rev. B*, 86(23):235304, December 2012. 2.2.2
- [51] I. Kudman. Thermoelectric properties of p-type PbTe-PbSe alloys. *Journal of Materials Science*, 7(9):10271029, 1972. 2.2.2
- [52] Yanzhong Pei, Xiaoya Shi, Aaron LaLonde, Heng Wang, Lidong Chen, and G. Jeffrey Snyder. Convergence of electronic bands for high performance bulk thermoelectrics. *Nature*, 473(7345):6669, May 2011. 2.2.2
- [53] Alan J. H. McGaughey. *Phonon transport in molecular dynamics simulations: Formulation and thermal conductivity prediction*. PhD thesis, University of Michigan, Ann Arbor, MI, 2004. 2.2.3, 2.3.3, A.8.1, A.8.2
- [54] Steve Plimpton. Fast parallel algorithms for short-range molecular dynamics. *Journal of Computational Physics*, 117(1):1–19, 1995. 2.2.3, A.8.2

- [55] Yuping He, Ivana Savic, Davide Donadio, and Giulia Galli. Lattice thermal conductivity of semiconducting bulk materials: Atomistic simulations. *Phys. Chem. Chem. Phys.*, page , 2012. 2.2.3, 2.3.3, 2.4
- [56] D. P. Sellan, J. E. Turney, A. J. H. McGaughey, and C. H. Amon. Cross-plane phonon transport in thin films. *Journal of Applied Physics*, 108:113524, 2010. 2.2.3, 2.5
- [57] J. D. Gale and A. L. Rohl. The general utility lattice program. *Molecular Simulation*, 29:291, 2003. 2.3.1, 2.3.2, 2.3.4, A.8.2
- [58] A. M. Bouchard, R. Biswas, W. A. Kamitakahara, G. S. Grest, and C. M. Soukoulis. Vibrational properties of amorphous silicon-germanium alloys and superlattices. *Phys. Rev. B*, 38(15):1049910506, November 1988. 2.3.1
- [59] John C. Duda, Timothy S. English, Donald A. Jordan, Pamela M. Norris, and William A. Soffa. Reducing thermal conductivity of binary alloys below the alloy limit via chemical ordering. *Journal of Physics: Condensed Matter*, 23(20):205401, 2011. 2.3.1, 2.3.2
- [60] Qian-Jin Chu and Zhao-Qing Zhang. Effect of correlations on the localization properties of electrons and phonons in the long-wavelength limit. *Phys. Rev. B*, 39(10):71207131, April 1989. 2.3.1
- [61] A. J. H. McGaughey, M. I. Hussein, E. S. Landry, M. Kaviany, and G. M. Hulbert. Phonon band structure and thermal transport correlation in a layered diatomic crystal. *Physical Review B*, 74:104304, 2006. 2.3.2, A.6.3, A.8.1
- [62] Yuping He, Davide Donadio, and Giulia Galli. Heat transport in amorphous silicon: Interplay between morphology and disorder. *Applied Physics Letters*, 98(14):144101, 2011. 2.3.2, 2.3.3
- [63] Davide Donadio and Giulia Galli. Atomistic simulations of heat transport in silicon nanowires. *Phys. Rev. Lett.*, 102(19):195901, May 2009. 2.3.2, 2.3.3
- [64] Takuma Hori, Takuma Shiga, and Junichiro Shiomi. Phonon transport analysis of silicon germanium alloys using molecular dynamics simulations. *Journal of Applied Physics*, 113(20):203514, 2013. 2.3.2, 2.3.3
- [65] S. Volz and G. Chen. Molecular-dynamics simulation of thermal conductivity of silicon crystals. *Physical Review B*, 61:26512656, 2000. 2.3.2
- [66] N. L. Green, D. Kaya, C. E. Maloney, and M. F. Islam. Density invariant vibrational modes in disordered colloidal crystals. *Physical Review E*, 83(5):051404, May 2011. 2.3.2
- [67] A. J. C. Ladd, B. Moran, and W. G. Hoover. Lattice thermal conductivity: A comparison of molecular dynamics and anharmonic lattice dynamics. *Physical Review B*, 34:50585064, 1986. 2.3.3, 2.3.3, A.1, A.2.1, A.3, A.3
- [68] J. E. Turney, E. S. Landry, A. J. H. McGaughey, and C. H. Amon. Predicting phonon properties and thermal conductivity from anharmonic lattice dynamics calculations and molecular dynamics simulations. *Phys. Rev. B*, 79(6):064301, February 2009. 2.3.3, 2.3.3, 2.3.3, 2.3.3, 2.3.3, 2.3.3
- [69] J. M. Larkin, J. E. Turney, A. D. Massicotte, C. H. Amon, and A. J. H. McGaughey. Comparison and evaluation of spectral energy methods for predicting phonon properties.

to appear in Journal of Computational and Theoretical Nanoscience, 2012. 2.3.3, 2.3.3, A.5

1949. 2.6

- [85] D. G. Cahill, W. K. Ford, K. E. Goodson, G. D. Mahan, A. Majumdar, H. J. Maris, R. Merlin, and S. R. Phillpot. Nanoscale thermal transport. *Journal of Applied Physics*, 93:793818, 2003. A.1
- [86] A. D. McConnell and K. E. Goodson. Thermal conduction in silicon micro and nanostructures. *Annual Review of Heat Transfer*, 14:129168, 2005. A.1
- [87] G. P. Srivastava. *The Physics of Phonons*. Adam Hilger, Bristol, 1990. A.1, A.2.1, A.3, A.5
- [88] D. C. Wallace. *Thermodynamics of Crystals*. Cambridge Univ. Press, Cambridge, UK, 1972. A.1, A.2.1, A.3, A.3
- [89] M. Asheghi, Y. K. Leung, S. S. Wong, and K. E. Goodson. Phonon-boundary scattering in thin silicon layers. *Applied Physics Letters*, 71:17981800, 1997. A.1
- [90] Alexander Balandin and Kang L. Wang. Significant decrease of the lattice thermal conductivity due to phonon confinement in a free-standing semiconductor quantum well. *Physical Review B*, 58(3):15441549, July 1998. A.1
- [91] S.-M. Lee and D. G. Cahill. Heat transport in thin dielectric films. *Journal of Applied Physics*, 81:25902595, 1997. A.1
- [92] Zhiting Tian, Keivan Esfarjani, Junichiro Shiomi, Asegun S. Henry, and Gang Chen. On the importance of optical phonons to thermal conductivity in nanostructures. *Applied Physics Letters*, 99(5):053122, 2011. A.1
- [93] A. I. Hochbaum, R. Chen, R. D. Delgado, W. Liang, E. C. Garnett, M. Najarian, A. Majumdar, and P. Yang. Enhanced thermoelectric performance of rough silicon nanowires. *Nature*, 451:163167, 2008. A.1
- [94] P. Martin, Z. Aksamija, E. Pop, and U. Ravaioli. Impact of phonon-surface roughness scattering on thermal conductivity of thin si nanowires. *Physical Review Letters*, 102:125503, 2009. A.1
- [95] Patrick E. Hopkins, Charles M. Reinke, Mehmet F. Su, Roy H. Olsson, Eric A. Shaner, Zayd C. Leseman, Justin R. Serrano, Leslie M. Phinney, and Ihab El-Kady. Reduction in the thermal conductivity of single crystalline silicon by phononic crystal patterning. *Nano Letters*, 11(1):107112, 2011. A.1
- [96] E. S. Landry and A. J. H. McGaughey. Effect of interfacial species mixing on phonon transport in semiconductor superlattices. *Physical Review B*, 79:075316, 2009. A.1
- [97] E. S. Landry and A. J. H. McGaughey. Effect of film thickness on the thermal resistance of confined semiconductor thin films. *Journal of Applied Physics*, 107:013521, 2010. A.1
- [98] M. G. Holland. Analysis of lattice thermal conductivity. *Physical Review*, 132:2461, 1963. A.1
- [99] A. J. H. McGaughey, E. S. Landry, D. P. Sellan, and C. H. Amon. Size-dependent model for thin film and nanowire thermal conductivity. *Applied Physics Letters*, 99:131904, 2011. A.1, A.9

